Revision 1
MS5563

Probing carbon-bearing species and CO_2 inclusion in amorphous carbon-$MgSiO_3$ enstatite reaction products at 1.5 GPa: Insights from ^{13}C high-resolution solid-state NMR

Kim, Eun Jeong[1]; Fei, Yingwei[2]; Lee, Sung Keun[1,*]

[1]School of Earth and Environmental Sciences
Seoul National University
Seoul, 151-742, Korea

[2]Geophysical Laboratory
Carnegie Institution of Washington
5251 Broad Branch Rd. N.W.
Washington D.C., 20015, USA

[*]Corresponding author,
Lee, Sung Keun
Professor
School of Earth and Environmental Sciences
Seoul National University
E-mail: sungklee@snu.ac.kr
Webpage: http://hosting03.snu.ac.kr/~sungklee
Phone: 82-2-880-6729
Fax: 82-2-871-3269

Submitted to 'American Mineralogist'
11-18-2015

ABSTRACT

Understanding the carbon speciation in earth materials is important to unravel the geochemical evolution of the earth's atmosphere, composition of partial melts, and overall distribution of carbon in the deep mantle. In an effort to provide the systematic protocols to characterize carbon-bearing fluid inclusions and other carbon-bearing species using high-resolution ^{13}C solid-state NMR, one of the element specific probe of local structure around carbon, we explore the atomic configurations around the carbon species formed during the reaction between ^{13}C-enriched amorphous carbon and $MgSiO_3$ enstatite synthesized at 1.5 GPa and 1400 °C using ^{13}C MAS NMR spectroscopy and Raman spectroscopy. The Raman spectra for the fluid inclusion show the presence of multiple molecular species (e.g., CO_2, CO, CH_4, H_2O, and H_2) and reveal heterogeneous distribution of these species within the inclusion. ^{13}C MAS NMR results show that the sharp peak at 125.2 ppm is dominant. While the peak could be assigned to either molecular CO_2 in the fluid phase or four-coordinated carbon ($^{[4]}C$), the peak is likely due to fluid CO_2, as revealed by Raman analyses of μm-size fluid inclusions in the sample. The peaks at 161.2, 170.9, and 173.3 ppm in the ^{13}C NMR spectrum correspond to the carbonate ions (CO_3^{2-}) and additional small peak at 184.5 ppm can be attributed to carbon monoxide. Based on the established relationship between ^{13}C abundance and peak intensity in the ^{13}C MAS NMR, the estimated ^{13}C amounts of CO_2, CO_3^{2-}, and CO species are much larger than those estimated carbon solubility in the crystals, thus, indicating that those carbon species are from external phases. The ^{13}C NMR spectrum for amorphous carbon showed a peak shift from ~ 130 ppm to ~ 95 ppm after compression, thereby suggesting that the amorphous carbon underwent permanent pressure-induced densification, characterized by the transition from sp^2 to sp^3 hybridization and/or pressure-induced changes in sp^2 carbon topology. While direct probing of carbon species

This is a preprint, the final version is subject to change, of the American Mineralogist (MSA)
Cite as Authors (Year) Title. American Mineralogist, in press.
(DOI will not work until issue is live.) DOI: http://dx.doi.org/10.2138/am-2016-5563

in the crystalline lattice using NMR is challenging, the current results and method can be utilized to provide quantitative analysis of carbon-species in the fluid-inclusions in silicates, which is essential for understanding the deep carbon cycle and volcanic processes.

Keywords: ^{13}C MAS NMR, enstatite, carbon speciation, amorphous carbon

INTRODUCTION

Understanding the carbon speciation in earth materials is important to unravel the geochemical evolution of the earth's atmosphere, composition of partial melts, and overall distribution of carbon in the deep mantle (Blank and Brooker, 1994; Green, 1972; Keppler et al., 2003; Richet and Bottinga, 1984; Shcheka et al., 2006; Zhang and Zindler, 1993). The properties of carbon-bearing crystalline silicates and their precursor liquids are also influenced by the amount of CO_2 present in these phases (Eggler and Kadik, 1979; Eggler and Rosenhauer, 1978). As the carbon-retention capacity of silicate melts and crystals depends heavily on pressure, decompression processes accompanied by eruption and upwelling of earth materials lead to the formation of exsolved CO_2 inclusions (Blundy et al., 2010; Eggler and Kadik, 1979; Lloyd et al., 2014; Parfitt and Wilson, 2008; Sides et al., 2014; Wallace, 2005).

H_2O and CO_2 are the most abundant volatile components in the Earth's interior. Additional species such as CH_4, H_2, and CO can be formed depending on total bulk chemistry of inclusion, f_{O2} condition, as well as temperature and pressure (e.g., Morizet et al., 2010; Mysen and Richet, 2005; Pawley et al., 1992). While the CO_2 inclusions are not included in an estimate of carbon solubility into silicate crystals and melts, they can contribute to the total bulk carbon contents of magma chambers, thereby affecting their buoyancy and rising speed (Blundy et

This is a preprint, the final version is subject to change, of the American Mineralogist (MSA)
Cite as Authors (Year) Title. American Mineralogist, in press.
(DOI will not work until issue is live.) DOI: http://dx.doi.org/10.2138/am-2016-5563

2010; Burton et al., 2013; Dixon and Clague, 2001; Gerlach et al., 2002; Kaminski and Jaupart, 1997; Lloyd et al., 2014; Parfitt and Wilson, 2008; Rust and Cashman, 2011; Sugioka and Bursik, 1995). For example, the exsolved CO_2 in Kilauea magma was estimated to be ~ 0.61 wt%, which is approximately 87% of the total CO_2 emitted from the volcanic eruption, while that of dissolved (and thus structurally-bound) CO_2 is ~ 0.09 wt% (Gerlach et al., 2002), indicating that the exsolved CO_2 in the glasses is among the important carbon reservoirs.

Together with CO_2 inclusions in the glasses, carbon species in crystalline silicates has been proposed as an additional carbon reservoir in the deep Earth (Green, 1972). Spectroscopic studies of vibrational density of states of species in fluid inclusion have provided useful information on the temperature-pressure conditions of the formation of the inclusion (Rosso and Bodnar, 1995; Seitz et al., 1996). In addition to the dissolved molecular CO_2 inclusions in the silicate crystals, neutral carbon may dissolve into the interstitial site in the crystal and/or dissolve into cation vacancies (Freund, 1981). Additionally, direct substitution of Si^{4+} with C^{4+} or with O^{2-} has also been suggested (Fyfe, 1970; Sen et al., 2013). However, revealing the mechanistic details of carbon incorporation into the crystalline silicates is challenging (Keppler et al., 2003; Shcheka et al., 2006).

Extensive previous studies using spectroscopic techniques such as Raman spectroscopy, Fourier-transform infrared spectroscopy (FTIR), as well as nuclear magnetic resonance spectroscopy (NMR) have revealed the speciation of carbon in silicate glasses (Blank et al., 1993; Brooker et al., 1999; Fine and Stolper, 1985; Kadik et al., 2004; Kohn et al., 1991; Morizet et al., 2002; Morizet et al., 2009; Morizet et al., 2010; Mysen, 2013; Mysen et al., 1975; Pawley et al., 1992; Richet and Bottinga, 1984; Stolper et al., 1987). While the Raman and FTIR techniques provide information on the collective vibration, solid-state NMR yields detailed, element-

This is a preprint, the final version is subject to change, of the American Mineralogist (MSA)
Cite as Authors (Year) Title. American Mineralogist, in press.
(DOI will not work until issue is live.) DOI: http://dx.doi.org/10.2138/am-2016-5563

specific, and quantitative information on the environment of nuclides of interest in the diverse crystalline and non-crystalline earth materials (e.g., Cody and Alexander, 2005; Cody et al., 2011; Feng et al., 2006; Kirkpatrick and Brow, 1995; Kirkpatrick et al., 1986; Lee, 2010; Papenguth et al., 1989; Phillips et al., 2000; Stebbins, 1995; Stebbins and Xue, 2014; Tangeman et al., 2001). Particularly, ^{13}C solid-state NMR has been used to determine the carbon speciation in synthetic silicate glasses with varying pressure and composition [e.g., Na-binary silicate glasses, Mg-binary silicate glasses, and CaO-MgO-Al_2O_3-SiO_2 (CMAS) silicate glasses, etc.] (Brooker et al., 1999; Jones et al., 2005; Kohn et al., 1991; Kwak et al., 2010; Morizet et al., 2002; Morizet et al., 2010). In contrast, the speciation of carbon in crystalline silicates has not been fully explored with the ^{13}C solid-state NMR techniques because carbon solubility into the crystals is often much lower than that into glasses and melts and NMR is one of the insensitive spectroscopic techniques. Additionally, the natural abundance of ^{13}C is only 1.1%, and the ^{13}C isotope enrichment is necessary. To the best of our knowledge, there is only a single ^{13}C NMR study of the carbon species in crystalline oxides (anatase TiO_2) where the sharp peak at 126 ppm was observed. On the basis of the usual peak position of orthocarbonate species in organic solids (121.0 ppm) (Pretsch et al., 2009), the peak was assigned to four-coordinated carbon ($^{[4]}C$) (Rockafellow et al., 2009). However, the 126 ppm peak could also be due to the exsolved CO_2 species in the oxides (Herzfeld and Berger, 1980; Kohn et al., 1991). Despite the difficulty, ^{13}C NMR can provide unique structural information around carbon species that is not accessible with other spectroscopic probes. For instance, the spinning sidebands patterns can be used to indicate whether CO_2 is structurally-incorporated or exsolved in silicate networks: CO_2 molecule in the inclusion may not show spinning sidebands while structurally-bound CO_2 can lead to the formation of spinning sideband patterns due to its large ^{13}C chemical shift anisotropy (Herzfeld

This is a preprint, the final version is subject to change, of the American Mineralogist (MSA)
Cite as Authors (Year) Title. American Mineralogist, in press.
(DOI will not work until issue is live.) DOI: http://dx.doi.org/10.2138/am-2016-5563

and Berger, 1980; Kohn et al., 1991).

Because the solubility of carbon into crystalline lattice is rather low (~ 0.1–5 ppm) and the amount carbon in fluid inclusion is also limited, direct probing of carbon species using NMR is challenging. While it is also currently difficult to detect the carbon signal, it would be useful to establish experimental protocols to further distinguish whether the observed NMR peaks are due to carbon species in the crystalline network or from the external phases (e.g., fluid inclusion, grain boundary etc.). Although solid-state NMR is not among the most sensitive spectroscopic techniques, we have made recent progress in probing (and detecting) dilute amount of nuclear spins in the earth materials under the extreme conditions (high pressure) using NMR (Lee, 2010; Lee, 2011; Lee et al., 2004; Lee et al., 2012). Furthermore, progress has been made to detect dilute nuclear spins in 2-dimensionally confined, 5 nm amorphous *thin* film (Lee and Ahn, 2014; Lee et al., 2009; Lee et al., 2010). These recent experimental achievements shed light on an opportunity to explore the dilute spins (such as ^{13}C in the inclusion and in the crystal) using high-resolution solid-state NMR. As few attempt to detect carbon species in the fluid inclusion or crystalline silicates has been reported, experimental verification of these species with practical detection limit for ^{13}C has been anticipated.

$MgSiO_3$ is the most abundant mineral composition in the mantle, which is likely to be the earth's largest carbon reservoir (Jambon, 1994; Shcheka et al., 2006). Enstatite is one of the $MgSiO_3$ phases stable in the crust and upper mantle. Here, we explore the atomic configuration around the carbon species formed during the reaction between ^{13}C amorphous carbon and enstatite synthesized at 1.5 GPa and 1400 °C using ^{13}C MAS NMR spectroscopy in order to test the utility of NMR technique to probe the carbon-bearing species in the reaction product and fluid inclusions. The study also aims to provide the systematic protocols to characterize

This is a preprint, the final version is subject to change, of the American Mineralogist (MSA)
Cite as Authors (Year) Title. American Mineralogist, in press.
(DOI will not work until issue is live.) DOI: http://dx.doi.org/10.2138/am-2016-5563

bearing fluid inclusion using high-resolution ^{13}C solid-state NMR. We also report the pressure-induced structural changes in the amorphous carbon that was used as a ^{13}C-enriched carbon reservoir in the high-pressure experiments. While the potential result can be helpful to provide comprehensive atomistic insights into the deep carbon cycle in the Earth's mantle, we also discuss the advantages and limitations of the NMR based strategy to detect 0.1–10 ppm of dissolved ^{13}C in crystalline silicates.

EXPERIMENTAL & COMPUTATIONAL METHODS

Sample preparation

The carbon-bearing enstatite samples for the spectroscopic analyses were synthesized by mixing $MgSiO_3$ (initially synthesized at 1.5 GPa) and ^{13}C-enriched amorphous carbon at 1.5 GPa. The starting $MgSiO_3$ enstatite was synthesized from a mixture of powdered SiO_2 and MgO in a Pt capsule using piston-cylinder apparatus with a 0.5" assembly at the Geophysical Laboratory, Carnegie Institution of Washington. The synthesis experiment was performed at 1400 °C and 1.5 GPa for 48 h. Subsequently, the enstatite was mixed with 2.4 wt% of ^{13}C-enriched (~ 99.7% enriched) amorphous carbon and H_2O, and then loaded in a Pt capsule. H_2O was added to promote the overall reaction and control the oxygen fugacity of the system [estimated oxygen fugacity was similar to that of C-CO (CCO) buffer (with estimated f_{O_2} value of ~ 7.5 D (Zhang and Duan, 2010). See Raman results below for details]. We then ran the experiments at 1.5 GPa and 1400 °C for 48 h to produce carbon-bearing enstatite. We have synthesized two distinct batches of samples under the same P-T conditions to check reproducibility of the carbon speciation in the synthesized samples. The formation of gas phases was observed when the capsule was opened after the experiments. This could be due to excess gas phases such as H_2O,

This is a preprint, the final version is subject to change, of the American Mineralogist (MSA)
Cite as Authors (Year) Title. American Mineralogist, in press.
(DOI will not work until issue is live.) DOI: http://dx.doi.org/10.2138/am-2016-5563

174 CO_2 or CH_4 (Mysen et al., 2009; Zhang and Duan, 2010). The resulting products included clear
175 carbon-bearing enstatite and black aggregated amorphous carbon (used as initial carbon source).
176 The latter, referred as compressed amorphous carbon, was handpicked and separated from the
177 enstatite. The decrepitation experiment was performed to identify the stability of the observed
178 carbon species and CO_2 inclusion in the sample: the synthesized $MgSiO_3$ grain [~ 80 μm (w) ×
179 100 μm (h)] with CO_2 inclusions were heated at 750 °C for 10 min in a tube furnace as previous
180 experimental studies often showed that the fluid inclusion in the crystal is not stable above
181 750 °C (Bodnar et al., 1989).
182
183 **Raman spectroscopy**
184 The Raman spectra for the carbon-bearing enstatite were collected on a micro Raman
185 spectrometer at Seoul National University. Thin-sections for Raman analysis were made by
186 fixing the enstatite particles in an epoxy resin. The enstatite crystals were polished using 1500
187 mesh diamond powder (8–10 μm) for 3 h and subsequently using 1 μm diamond paste for 1 h.
188 The spectra were collected under the following conditions: laser wavelength of 488 nm, exposure
189 time of 10 s, and number of accumulation being 60 with grating groove density of 1800/500
190 L/mm. The spectral resolution is ~ 0.55–0.85 cm^{-1}/pixel and the spectrometer slit width is 250
191 μm. Typical spectral width is ~ 840 cm^{-1} (centered at 1400 cm^{-1})and ~ 780 cm^{-1} (centered at 2250
192 cm^{-1}), respectively. Beam diameter of 3.1 μm (using 50× microscope objectives), laser power of
193 32.8 mW, and beam scattering of 1 mrad were used. An estimated reproducibility in recorded
194 peak positions of the current spectra is less than ± 0.5 cm^{-1}.
195
196 **NMR spectroscopy**

The ^{13}CMAS NMR spectra were collected on a Varian 400 MHz solid-state NMR spectrometer (9.4 T, Seoul National University) at a Larmor frequency of 100.582 MHz for ^{13}C using a 3.2 mm zirconia rotor in a Varian double-resonance probe. It may require longer relaxation delays to obtain the fully relaxed spectrum for the carbon-bearing enstatite. We therefore performed ^{13}C MAS NMR experiments with varying relaxation delay times. The results showed negligible effect on the different relaxations of carbon peaks. Therefore, the recycle delay of 5 s was used to reduce the total NMR collection time. The magic-angle sample spinning speed of 14 kHz was employed. The current signal-to-noise ratio in the spectra was achieved by averaging nearly 86400 scans (~ 5 days). The spectra were referenced to solid-state adamantane (ADM, $C_{10}H_{16}$), whose resonance of left peak was located at 38.56 ppm relative to the more common reference, tetramethylsilane (TMS). Approximately 20 mg of carbon-bearing $MgSiO_3$, 1.7 mg of ^{13}C-enriched uncompressed amorphous carbon, and 3.2 mg of ^{13}C-enriched compressed amorphous carbon were used in the ^{13}C MAS NMR experiments. The background signals were collected under identical measurement conditions using an empty zirconia rotor. The background spectrum was subsequently subtracted from the ^{13}C MAS NMR spectrum for each sample to yield the NMR spectrum free from any background carbon signals.

^{13}C NMR spin-counting experiment was performed using mixtures of ADM and SiO_2 (Sigma-Aldrich product no. 204358). We collected ^{13}C MAS NMR spectra for the mixtures with varying ADM/SiO_2 ratio [X_{ADM} = 1/4 (25 wt%, 2750 ppm of ^{13}C), 1/8 (12.5 wt%, 1375 ppm of ^{13}C), 1/16 (6.25 wt%, 688 ppm of ^{13}C), 1/50 (2.0 wt%, 220 ppm of ^{13}C), 1/233 (0.43 wt%, 47 ppm of ^{13}C), 1/310 (0.32 wt%, 35 ppm of ^{13}C)]. The mixtures were ground in an agate mortar for 1 h. It is somewhat difficult to constrain the composition of the mixtures with low ADM concentration (e.g., the data for X_{ADM}=1/50, 1/233, and 1/310). This is due to uneven

This is a preprint, the final version is subject to change, of the American Mineralogist (MSA)
Cite as Authors (Year) Title. American Mineralogist, in press.
(DOI will not work until issue is live.) DOI: http://dx.doi.org/10.2138/am-2016-5563

between ADM and SiO_2 in the mortar stemming from the difference in surface adhesiveness of the ADM and SiO_2 particles. Therefore, in order to minimize the ADM loss upon mixing in the agate mortar (i.e., to yield better calibration curve), a designed amount of ADM was located at the center of the rotor and SiO_2 powder was placed both on top and bottom of the rotor. The NMR collection conditions for the mixtures were identical to those for carbon-bearing enstatite.

As elemental analysis does not provide robust measurement of the carbon content in SiO_2-ADM mixture used in the study primarily due to difference in volatilization between ADM and SiO_2, the quantitative carbon content of the mixture with low carbon concentration was constrained using the calibration curve (between NMR peak intensity and carbon content) based on the mixture with higher concentration (see discussion below). The NMR experiment under proton decoupling was also performed to improve the quality of ^{13}C abundance and peak intensity calibration curve. Proton decoupling power was optimized using ADM standard. The spectra for the mixtures were collected at a decoupling power $\omega_1/2\pi$ of 33 kHz.

Quantum chemical calculations

Quantum chemical calculations of NMR chemical shift of $C(OH)_4$ clusters were performed using Gaussian 03 in order to get insights into the ^{13}C NMR chemical shielding for $^{[4]}C$ with varying C-O bond lengths (Frisch et al., 2004). A model $C(OH)_4$ cluster was optimized by varying the C-O bond lengths while maintaining the tetrahedral symmetry constraints at the Becke, three-parameters, Lee-Yang-Parr (B3LYP) level of theory with a 6-311+G(2d) basis set. The NMR chemical shielding calculations of the C atoms in $C(OH)_4$ cluster were calculated using the gauge-including atomic orbital (GIAO) method at the B3LYP level of theory with the 6-311G+(2d) and 6-31G(d) basis sets (Lee and Lee, 2009). The ^{13}C NMR chemical shift of the

243 $C(OH)_4$ cluster was estimated by subtracting NMR chemical shielding of TMS (external
244 reference used in the experiment) that was also calculated at the identical energy level of theory
245 and basis sets.
246
247 ## RESULTS
248 **Probing of CO_2 in fluid inclusions in carbon-bearing enstatite: Insights from Raman**
249 **spectroscopy**
250 Figure 1 shows the optical micrograph image of the sample (Figure 1 a, grain size of
251 approximately 80 μm (w) × 100 μm (h)] and Raman spectrum for the observed fluid inclusion [4
252 μm (w) × 10 μm (h)] (Figure 1 b, c, d). The Raman spectra for the fluid inclusion (Fig. 1 b) show
253 the presence of multiple molecular species (e.g., CO_2, CO, CH_4, H_2O, and H_2) and reveal
254 heterogeneous distribution of these species within the inclusion. The peaks at 1280 and 1380 cm^{-1}
255 correspond to the symmetric stretching vibration (v_1) and the overtone of the symmetric
256 bending ($2v_2$) vibrations in CO_2 (Morizet et al., 2009), and those at 2100 cm^{-1} and 3000–3800
257 cm^{-1} are due to CO and H_2O (Morizet et al., 2009; Mysen et al., 2011), respectively. The peaks at
258 2912 and 4150 cm^{-1} originate from CH_4 and H_2, respectively (Mysen et al., 2009).
259 Figure 1 c and d shows further details of characteristic of vibrational modes of CO_2 and
260 CO, respectively. The two peaks at 1360 cm^{-1} and 1385 cm^{-1} in Fig. 1 c are characteristic of the
261 overtone of the symmetric bending ($2v_2$) vibrations of $^{13}CO_2$ and $^{12}CO_2$ in the fluid inclusions
262 while the two peaks at 1260 cm^{-1} and 1285 cm^{-1} correspond to the symmetric stretching (v_1)
263 vibrations of $^{13}CO_2$ and $^{12}CO_2$, respectively (Ni and Keppler, 2013). The peak at 1405 cm^{-1}
264 represents the hot band vibration of the low-lying vibration of v_2 at 667.38 cm^{-1} (Rosso and
265 Bodnar, 1995). Figure 1 d indicates the presence of minor but detectable ^{13}CO and ^{12}CO species

This is a preprint, the final version is subject to change, of the American Mineralogist (MSA)
Cite as Authors (Year) Title. American Mineralogist, in press.
(DOI will not work until issue is live.) DOI: http://dx.doi.org/10.2138/am-2016-5563

in the fluid inclusion at 2090 $cm^{-1}$and 2140 cm^{-1}, respectively (Morizet et al., 2009). These Raman features for CO and CO_2 were not observed within the inclusion-free enstatite crystals. The coexistence of these fluid species can correspond to f_{O2} ranging from -7.14 to -10.88 (calculated using the GFluid code), similar to those with C-CO buffer (f_{O2} = ~ -7.5) (Zhang and Duan, 2010).

The internal pressure in the fluid inclusion have been estimated from the frequency difference in upper band and lower band of CO_2 (i.e., v_1-2v_2) (Garrabos et al., 1989; Kobayashi et al., 2012; Rosso and Bodnar, 1995; Seitz et al., 1996; Wright and Wang, 1973). Alternatively, the peak position of v_1 vibration of CH_4 at room temperature has also been utilized to obtain internal pressure (Lin et al., 2007; Seitz et al., 1996). As we have not collected the Raman spectrum for the inclusion with varying temperature, taking into consideration sources of uncertainty and potential complications in the previous calibration curve, the difference in CO_2 bands (104.2–104.7 cm^{-1}) may not be directly used to provide robust pressure conditions in the current study. In order to estimate the internal pressure of the fluid inclusion from the CH_4 peak positions in the Raman spectrum, the exact composition of the inclusion needs to be known. As the chemical composition of the inclusion is currently not clear, a quantitative estimation of the internal pressure is not straightforward. Roughly, the current peak position of CH_4 (2911.5–2912.2 cm^{-1}) corresponds to the internal pressure of ~ 100–200 bar (e.g. if X_{CH4} = ~ 0.1 in CH_4–CO_2 mixture). Further detailed study with in-situ high-temperature Raman analyses is necessary for robust estimation of internal pressure.

While Raman spectroscopy may not be fully quantitative, previous extensive Raman studies of fluid inclusions in silicate glasses highlighted that quantitative estimation of carbon species concentration is indeed possible, once their respective peak intensity was calibrated

This is a preprint, the final version is subject to change, of the American Mineralogist (MSA)
Cite as Authors (Year) Title. American Mineralogist, in press.
(DOI will not work until issue is live.) DOI: http://dx.doi.org/10.2138/am-2016-5563

the Raman efficiency for each molecule established from the standard samples with controlled concentrations (Burke, 2001; Morizet et al., 2009). The method is not applied for the samples studied here due mainly to difficulties in establishing the Raman efficiency of the species with the spectrometer used in the current study (mostly due to lack of heating stage, standard samples with known concentrations of molecular species, and heterogeneous distribution of carbon-bearing species in the inclusion). Nevertheless, this earlier approach, combined with NMR, is potentially useful to provide quantitative information of fluid composition and species concentration.

Probing of carbon species and inclusion in carbon-bearing enstatite: ^{13}C MAS NMR results

Figure 2 shows the ^{13}C MAS NMR spectrum for carbon-bearing enstatite. Because the ^{13}C MAS NMR spectrum of the empty rotor shows the presence of a detectable amount of carbon background signal from the rotor and stator ranging from 100–170 ppm (Fig. 2 bottom), the background signal was subtracted from the collected spectrum (Fig. 2 middle). The top spectrum in Figure 2 shows the background-subtracted ^{13}C MAS NMR spectrum for the sample. The background-subtracted spectrum shows multiple sharp peaks at 184.5, 173.3, 170.9, 161.2, and 125.2 ppm, which can be attributed to the distinct carbon species in enstatite. The sharp peak at 125.2 ppm is prevalent. Based on the NMR chemical shift of the peak, it could be attributed to either molecular CO_2 in fluid phase, structurally bound CO_2 in silicate network, or $^{[4]}$C (Herzfeld and Berger, 1980; Kohn et al., 1991; Rockafellow et al., 2009). While the origin of the peak at 125.2 ppm in carbon-bearing enstatite will be discussed, the peak is mostly due to molecular CO_2 on the basis of its narrow peak width with negligible spinning sideband intensity and insights

311 from the quantum chemical calculations (see discussion discussion below for further details).
312 This assignment is also consistent with the aforementioned Raman results (Fig. 1).

313 The 161.2, 170.9, and 173.3 ppm peaks correspond to the carbonate ions (CO_3^{2-}) on the
314 basis of previous studies of carbonate species in the silicate glasses (e.g., Brooker et al., 1999;
315 Kohn et al., 1991; Mysen et al., 2011). Additionally, chemical shifts for carbonate minerals (e.g.,
316 calcite, magnesite, vaterite, dolomite, lithium carbonate, sodium carbonates, and cerussite) also
317 range from 166–171 ppm (Papenguth et al., 1989). Previous quantum simulations of ^{13}C
318 NMR chemical shift in aluminosilicate glasses showed that the distortion of CO_3^{2-} cluster
319 decrease in the ^{13}C NMR chemical shift (Tossell, 1995), as also suggested from an earlier NMR
320 study (Brooker et al., 1999). The simulations also indicated that highly distorted carbonate ions
321 with C-O bond length of 1.265 Å, which was shorter than the average bond lengths of the
322 carbonate minerals (1.285 Å), have smaller NMR chemical shift (Tossell, 1995). The additional
323 small peak at 184.5 ppm observed in the spectrum (Fig. 2) can be attributed to carbon monoxide
324 (Kohn et al., 1991; Tossell, 1995). Figure 3 also shows the ^{13}C MAS NMR spectra for carbon-
325 bearing enstatite synthesized at 1.5 GPa and 1400 °C, and that annealed at 750 °C for 10 min.
326 Upon annealing, the ^{13}C MAS NMR spectrum for the annealed carbon-bearing enstatite did not
327 show the presence of carbon species (Fig. 3 bottom). This suggests that the carbon species in
328 enstatite are not stable upon annealing at 750 °C.

329 On the basis of the relationship between peak area and ^{13}C abundance (see discussion
330 4.3), we should note that the amount of ^{13}CO and $^{13}CO_3^{2-}$ are much larger than the reported
331 solubility of carbon (including ^{12}C and ^{13}C) into enstatite (~ 0.05–4.7 ppm) (Keppler et al., 2003;
332 Shcheka et al., 2006) (see appendix A1 for the previously estimated solubility of carbon species
333 in crystalline silicates at high pressure). Therefore, the observed carbonates and CO species

This is a preprint, the final version is subject to change, of the American Mineralogist (MSA)
Cite as Authors (Year) Title. American Mineralogist, in press.
(DOI will not work until issue is live.) DOI: http://dx.doi.org/10.2138/am-2016-5563

the spectra are not likely due to carbon species in enstatite crystalline network, rather these stem from external reaction products formed during sample synthesis.

The Raman spectra show the presence of CH_4 in the fluid inclusion (Fig. 1 b). Because the potential peak position for CH_4 species somewhat overlaps with the spinning side bands of the probe background signal (at 14 kHz), ^{13}C MAS NMR spectra for the sample were collected with varying spinning speed (11 and 14 kHz). A small feature at ~ -9 ppm is observed in ^{13}C MAS NMR spectra at 11 kHz (Fig. 4). Previous study of carbon-bearing Na_2O-$4SiO_2$ glass synthesized at 1.5 GPa and 1400°C reported a sharp peak due to CH_4 species at -5.4 ppm in the ^{13}C MAS NMR (Mysen et al., 2011). Figure A1 in appendix A2 shows ^{13}C MAS NMR spectrum for carbon-bearing enstatite under proton decoupling where any expected decrease in the peak width for the peak ~ -9 ppm is not shown, indicating that the carbon species responsible for -9 ppm peak does not have clear proximity toward hydrogen. ^{1}H MAS NMR spectrum for carbon-bearing enstatite shows the presence of CH_4 species at ~ 0.3 ppm (not shown here) (Pretsch et al., 2009). The result, therefore, indicates that the feature at ~ -9 ppm in ^{13}C MAS NMR spectra is mostly due to the probe background signal and the observed CH_4 in the Raman spectrum is likely due to the ^{12}C infiltrated from the graphite heater (Brooker et al., 1998; Cerfontain et al., 1987).

Pressure-induced structural changes of amorphous carbon: Insights from ^{13}C MAS NMR

Because we used ^{13}C-enriched amorphous carbon as a carbon reservoir, the current NMR experiment for amorphous carbon can also provide insights into the effect of pressure on the structure of amorphous carbon. Figure 5 (a) shows the background-subtracted ^{13}C MAS NMR spectra for the compressed and uncompressed ^{13}C-enriched amorphous carbon. The ^{13}C NMR spectrum for amorphous carbon shows a broad peak at ~ 130 ppm. After compression at

This is a preprint, the final version is subject to change, of the American Mineralogist (MSA)
Cite as Authors (Year) Title. American Mineralogist, in press.
(DOI will not work until issue is live.) DOI: http://dx.doi.org/10.2138/am-2016-5563

1.5 GPa and 1400 °C for 48 h, the spectrum for the compressed amorphous carbon shows a broad peak at ~ 95 ppm. The observed pressure-induced changes in the peak position of amorphous carbon in the ^{13}C NMR spectra (Fig. 5) may stem from multiple distinct structural changes upon compression, which includes bonding transition from sp^2 to sp^3 states. This could also be due to incorporation of hydrogen into carbon stemming from H_2O added during synthesis and the pressure-induced changes in network topology without changes in bonding states.

As the peak position for the typical carbon species with sp^2 and sp^3 bonding are ~ 138 ppm and ~ 68 ppm, respectively (Alam et al., 2002; Cho et al., 2008), this observation may indicate that the uncompressed amorphous carbon contains more sp^2 hybridized carbon species, while the compressed amorphous carbon at 1.5 GPa has more sp^3 hybridized carbon; amorphous carbon undergoes permanent pressure-induced densification, characterized by the transition from sp^2 to sp^3 hybridization. Alternatively, the previous studies have also shown that chemical shift and peak positions for sp^2 carbon varies with varying carbon network topology. Table 1 shows the ^{13}C NMR chemical shifts (and peak positions) of various carbon species in amorphous and crystalline carbon phases and allotropes. These phases have distinct network topology, yet consisting only of carbons with sp^2 bonding orbitals. While NMR chemical shift for sp^3-like carbon varies from 62 to 67.5 ppm (Alam et al., 2003; Pan et al., 1991), those for sp^2-like carbons also range from 102.3 to 149.7 ppm and are dependent on network topology; for example, the chemical shift of carbon in carbon nanotubes decreases with increasing the number of walls (Abou-Hamad et al., 2011). The peak positions of aromatic C=C bonds in graphene and carbon black is 123–126 ppm (Jäger et al., 1999; Si and Samulski, 2008). The chemical shift for fullerene C_{60} is 142.6 ppm and that for fullerene C_{70} shows multiple sharp peaks at 129.9 ppm, 144.7 ppm, 146.9 ppm and 149.7 ppm; all those crystallographically distinct carbon sites have

This is a preprint, the final version is subject to change, of the American Mineralogist (MSA)
Cite as Authors (Year) Title. American Mineralogist, in press.
(DOI will not work until issue is live.) DOI: http://dx.doi.org/10.2138/am-2016-5563

varying symmetry and topology (Kanowski et al., 1997; Taylor et al., 1990).

Therefore, while the observed peak shift in the ^{13}C MAS NMR spectrum for the amorphous carbon (Fig. 5) can certainly be due to changes in sp^2 to sp^3 hybridization that was also previously reported at higher pressure upon *cold* compression (Lin et al., 2011), it could also stem from the pressure-induced changes in carbon topology while maintaining sp^2 bonding state as shown in Table 1. Further experimental and theoretical confirmations are necessary. Finally, while the observed shift may be due to the effect of residual hydrogen, taking into consideration negligible hydrogen content in the compressed amorphous carbon as evidenced by the ^1H NMR spectra, the pressure-induced peak shift is not affected by the proton in the sample (see appendix A3).

We note that the NMR signal is comparable to that of background signal; Figure 5 (b) and (c) show the ^{13}C MAS NMR spectra for ^{13}C-enriched uncompressed and compressed amorphous carbon and those for rotor and stator backgrounds. The observed difference in signal-to-noise ratio between the two spectra (uncompressed vs. compressed) are due to the absolute intensity differences in the two samples because of possible difference in spin-lattice relaxation times and/or the potential paramagnetic interaction between unpaired electron and ^{13}C nuclides in the amorphous carbons: roughly, the calibration curve between ^{13}C NMR peak intensity and ^{13}C concentration based on the spin-counting experiment (see section 4.3 below), the peak intensity of compressed amorphous carbon corresponds to only ~ 20% of ^{13}C in the sample. It is currently difficult to distinguish the effect of paramagnetic interaction from the contribution from the spin-lattice relaxation times (T_1) mostly because of difficulty in estimating T_1 time for the compressed carbon.

This is a preprint, the final version is subject to change, of the American Mineralogist (MSA)
Cite as Authors (Year) Title. American Mineralogist, in press.
(DOI will not work until issue is live.) DOI: http://dx.doi.org/10.2138/am-2016-5563

In order to yield the background-subtracted spectra, the intensity of the background signal was adjusted (~ 80%) by matching the sharp peak intensity at ~ 170 ppm. A decrease in the background intensity of the ^{13}C MAS NMR spectra for the compressed and uncompressed amorphous carbon is likely due to the presence of the unpaired electrons in both samples [as expected from the presence of sp^2 bonding (Cho et al., 2008)]. While the current result is the first-of-its-kind observation of the pressure-induced permanent structural changes in amorphous carbon using ^{13}C MAS NMR, the effect of paramagnetic interaction (between unpaired electron and ^{13}C nuclides) remains to be fully established.

DISCUSSION

Origin of peak at 125.2 ppm in carbon-bearing enstatite

The current ^{13}C NMR spectrum shows a strong and sharp resonance peak at 125.2 ppm. The FWHM of the peak is approximately 0.6 ppm with an applied Gaussian broadening factor of 0.01. While the ^{13}C NMR studies of carbon phases in the crystalline silicates have not been performed hitherto, previous studies on the ^{13}C MAS NMR for carbon-bearing anatase TiO_2 proposed that the extremely sharp peak at 126 ppm can be attributed to $^{[4]}C$ in crystalline TiO_2 (Rockafellow et al., 2009). Alternately, in the previous ^{13}C NMR study of the carbon species in the sodium aluminosilicate glasses, the peak at ~125 ppm with the spinning sidebands was assigned to the dissolved molecular CO_2 in the glass network (Kohn et al., 1991). The dissolved CO_2 molecules bound to the crystalline/non-crystalline silicate networks would be subject to the low degree of freedom. This leads to a relatively large ^{13}C NMR chemical shift anisotropy of ~ 260–270 ppm (Herzfeld and Berger, 1980), resulting in the visible spinning sidebands (Kohn et al., 1991). In contrast, the CO_2 molecules in micro-fluid inclusions, which were not strongly

This is a preprint, the final version is subject to change, of the American Mineralogist (MSA)
Cite as Authors (Year) Title. American Mineralogist, in press.
(DOI will not work until issue is live.) DOI: http://dx.doi.org/10.2138/am-2016-5563

425 bound to the networks, may not show spinning sidebands (Herzfeld and Berger, 1980; Kohn et
426 al., 1991). If the CO_2 is bound to the enstatite network, the spinning sidebands of the CO_2 peak
427 should appear at approximately 265 ppm and -15 ppm in the current ^{13}C MAS NMR spectrum.
428 However, the spinning sidebands for the CO_2 peak were not observed in the current study.
429 Therefore, the observed peak at 125.2 ppm in the current ^{13}C MAS NMR spectrum is likely to
430 result from the fluid-phase CO_2 molecule in the inclusion as also indicated by the presence of
431 CO_2 band in the Raman spectrum (Fig. 1). While an experimental artificial signal (central spike)
432 may overlap with the peak at 125.2 ppm in the previous pioneering study (Kohn et al., 1991), the
433 current ^{13}C NMR experiments were performed with the varying carrier frequency. The result
434 confirms that the peak at 125.2 ppm is not due to the additional artifact signal. We also
435 synthesized the sample twice using the identical experimental conditions in the piston cylinder to
436 substantiate the reproducibility: the ^{13}C MAS NMR spectra for both samples also showed a sharp
437 peak at 125.2 ppm.
438
439 **^{13}C NMR chemical shift for orthocarbonate species ($^{[4]}C$): Insights from quantum chemical**
440 **calculations**
441 A previous study suggested that the peak at ~ 120 ppm can be assigned to $^{[4]}C$
442 (Rockafellow et al., 2009). The peak position also corresponds to suggested peak position for
443 molecular CO_2 (e.g., Brooker et al., 1999; Kohn et al., 1991; Morizet et al., 2010; Mysen et al.,
444 2011). In order to confirm these earlier peak assignments, theoretical confirmation is required.
445 Here, we calculated the chemical shift of $^{[4]}C$ [$C(OH)_4$ cluster] using quantum chemical
446 calculations. The theoretical calculation of NMR chemical shielding tensor for the model $C(OH)_4$
447 cluster shows the effect of the C-O bond length of $^{[4]}C$ cluster on the ^{13}C chemical shift (Fig.

This is a preprint, the final version is subject to change, of the American Mineralogist (MSA)
Cite as Authors (Year) Title. American Mineralogist, in press.
(DOI will not work until issue is live.) DOI: http://dx.doi.org/10.2138/am-2016-5563

448 The calculated ^{13}C NMR chemical shift is also dependent on the energy level of theory and the
449 basis sets used. Here the calculations were performed at the B3LYP level of theory with a 6-
450 311+G(2d) basis set that reproduced experimental ^{13}C chemical shifts for the known molecules
451 relatively well (Kim and Lee, 2011; Lee and Lee, 2009). For example, the calculated NMR
452 chemical shift for the CO_2 molecule is 125.7 ppm at the B3LYP level of theory with a 6-
453 311+G(2d) basis set (Kim and Lee, 2011). The chemical shift is consistent with the result from
454 experimental ^{13}C liquid-state static NMR spectrum of CO_2 gas molecule (Ettinger et al., 1960).
455 The calculated NMR chemical shift also varies with basis sets used. For instance, the shift of
456 CO_2 molecule calculated at the B3LYP/6-31G(d) is 108.807 ppm (Kim and Lee, 2011).

457 Figure 6 shows that the effect of the C-O bond length on a single point energy and NMR
458 chemical shift. The quantum chemical calculations of $C(OH)_4$ cluster with an equilibrium C-O
459 bond length of 1.388 Å [calculated at the B3LYP/6-311+G(2d)] show that the chemical shift is
460 117.451 ppm. The calculated NMR chemical shift of $C(OH)_4$ cluster gradually increases with
461 increasing the C-O bond length. The ^{13}C chemical shift increases from 121.2 ppm at 1.40 Å to
462 196.9 ppm at 1.60 Å. In the previous report, we also showed that the $^{[4]}C$ peak with a C-O bond
463 length of 1.60 Å (if C substitutes Si in the chain silicate network) leads to a chemical shift of
464 254.6 ppm (Kim and Lee, 2011).

465 If the C-O bond length of the $^{[4]}C$ cluster in the enstatite were ~ 1.388 Å, the peak
466 position of the $^{[4]}C$ species would be ~ 117.451 ppm. Therefore, taking into consideration the
467 similarity between the chemical shifts for CO_2 and $^{[4]}C$, it is difficult to assign the peak based
468 only on the ^{13}C chemical shift. In the current study, as we observed CO_2-rich fluid inclusions
469 confirmed by Raman spectroscopy (Fig. 1), the peak at 125.2 ppm in the current ^{13}C MAS NMR
470 spectrum is likely to be the free CO_2 molecule in enstatite.

This is a preprint, the final version is subject to change, of the American Mineralogist (MSA)
Cite as Authors (Year) Title. American Mineralogist, in press.
(DOI will not work until issue is live.) DOI: http://dx.doi.org/10.2138/am-2016-5563

471

472 **External *vs.* structurally-incorporated carbon species in the carbon-bearing enstatite:**
473 **Insights from quantitative ^{13}C spin counting experiment using ADM-SiO_2 mixture**

474 **Calibration curve between ^{13}C abundance and ^{13}C MAS NMR peak intensity.** In order to
475 evaluate whether the observed ^{13}C NMR peaks stem from the structurally-incorporated carbons
476 in the enstatite or those in external phases, it is necessary to estimate the solubility of carbon in
477 enstatite and to perform quantitative measurement of the amount of carbon species in carbon-
478 bearing enstatite in ^{13}C MAS NMR spectra (Fig. 2), and finally to compare the estimated amount
479 of carbon in enstatite with the solubility of carbon in enstatite. A clear linear relationship
480 between peak intensity and concentration was established for X_{ADM}=1/4, 1/8 and 1/16. We then
481 extrapolated the trend line obtained from the samples with these higher ADM concentration to
482 the samples with lower ADM concentration. The NMR intensity data for the samples with the
483 lower ADM concentration were then adjusted to match the extrapolated line. This allows us to
484 estimate the carbon concentration in the carbon-poor sample. The estimated carbon
485 contents from the calibration curve are 2.0 wt% (220 ppm of ^{13}C) for X_{ADM}=1/50 sample; 0.43
486 wt% (47 ppm of ^{13}C) for X_{ADM}=1/233 sample; and 0.32 wt% (35 ppm of ^{13}C) for
487 X_{ADM}=1/310 sample, respectively. We note again that the carbon content of the mixture with low carbon concentration
488 was estimated using its peak intensity and established calibration curve for the mixtures with
489 higher carbon concentration, while this may not be fully desirable. This is mainly because of the
490 aforementioned difficulty in homogeneous mixing between a small amount of ADM and SiO_2
491 and partly due to their differences in volatilization during elemental analysis. Nevertheless, NMR
492 peak intensity does correspond to robust carbon content and thus allows for rigorous estimation
493 of amount of carbon in the mixtures.

This is a preprint, the final version is subject to change, of the American Mineralogist (MSA)
Cite as Authors (Year) Title. American Mineralogist, in press.
(DOI will not work until issue is live.) DOI: http://dx.doi.org/10.2138/am-2016-5563

Figure 7 (top) shows ^{13}C MAS NMR spectra for ADM-SiO_2 mixtures with varying X_{ADM}. The peak area in each spectrum decreases with decreasing X_{ADM}. Figure A3 in appendix A4 shows the ^{13}C MAS NMR spectra for ADM-SiO_2 mixtures with varying X_{ADM} ratio under proton decoupling. The spectra show that proton decoupling indeed improves signal-to-noise ratio while the peak intensity is conserved. We also note that the carbon species (including CO_2, CO_3^{2-}) that do not have hydrogen bonded to carbon may not undergo enhancement in signal-to-noise ratio further. Figure 7 (bottom) shows the relationship between the ^{13}C MAS NMR peak intensity and the estimated ^{13}C abundance in ADM-SiO_2 mixtures. The linear correlation between the ^{13}C abundance (X) in the ADM-SiO_2 mixture and the normalized peak intensity (Y, normalized with respect to that of X_{ADM}=1/4.) in ^{13}C MAS NMR spectra can be established: Y=0.0369X.

Effect of spin-lattice relaxation time. While we used the ADM-SiO_2 mixtures as an analog for the carbon species in the compressed silicates, the spin-lattice relaxation times for ADM and carbon species in the compressed enstatite are different: the T_1 for the latter is longer than that of the former. Because of the differences in spin-lattice relaxation times, the actual carbon concentration (particularly that of carbonate species) in the sample can be higher from those estimated here: T_1 of ADM is ~ 1 s (Resing, 1969) and thus the current recycle delay of 5 s provides quantitative insight into the carbon content in the sample. As for the other carbon species, due to low spin density, the T_1 for the CO_2 has not been estimated. Nevertheless, the previous studies have shown that spin-lattice relaxation time of gas phase CO_2 varies from ~ 0.2 sec at an internal pressure of 10.3 bar, 16.34 sec at 137.89 bar, and to ~ 22 sec at an internal pressure of 413.68 bar (Etesse et al., 1992). While the T_1 for CO_2 varies with the density, the ^{13}C MAS NMR experiment with 5 s and 40 s delay times does not lead to a noticeable difference in signal intensity. Therefore, the current results with 5 s relaxation delay provide moderately

This is a preprint, the final version is subject to change, of the American Mineralogist (MSA)
Cite as Authors (Year) Title. American Mineralogist, in press.
(DOI will not work until issue is live.) DOI: http://dx.doi.org/10.2138/am-2016-5563

517 robust estimation of CO_2 content in the glasses. As for the CO_3^{2-} species, the estimated T_1 values
518 for Na_2CO_3 and $CaCO_3$ are ~ 1729 and 6418 s, respectively. That for $MgCO_3$ magnesite is ~ 78 s
519 (Moore et al., 2015). Thus the calibration curve based on ADM may not provide robust and
520 quantitative estimation of the carbonate content in the current sample, particularly. The predicted
521 $^{13}CO_3^{2-}$ content is likely to be smaller than the actual content.
522 **Estimated carbon contents.** The estimated minimum ^{13}C abundance from ^{13}C MAS NMR
523 spectra for ADM-SiO_2 mixture is ~ 35 ppm of ^{13}C from the calibration curve based on ^{13}C MAS
524 NMR experiments. Based on the established calibration curve, we believe that the detection limit
525 is ~ 5–10 ppm for ^{13}C species with the employed instrumentation and the experimental
526 conditions in the current study (~ 5 days of signal averaging at 9.4 T static field with a rf field
527 strength of 66.7 kHz in the 3.2 mm rotor with full sample volume of ~ 19 mm^3). Whereas the
528 spin-lattice relaxation times, particularly carbonates species in the enstatite-amorphous carbon
529 reaction products need to be estimated, because of the limited sample volume, it is currently
530 challenging to measure T_1. Nevertheless, based on the calibration curve, the estimated
531 ^{13}C amounts of CO_2, CO_3^{2-}, and CO species are ~ 142–166 ppm, ~ 28–45 ppm (once calibrated
532 with T_1 effect, the concentration should be higher than the current value), and ~ 6–7 ppm, respectively.
533 The previously reported solubility of carbon species in enstatite is 0.05–4.7 ppm (Keppler et al.,
534 2003; Shcheka et al., 2006); therefore the estimated carbon contents from the NMR spectra
535 indicate that those carbon species are from external phases.
536 **External crystalline carbonate phases.** Characteristic vibrational frequencies for calcite and
537 magnesite are expected to be at 1088 cm^{-1} and 1095 cm^{-1}, respectively. We note that there is also
538 an expected peak shift toward higher frequency with increasing pressure. C-O asymmetric
539 stretching vibration for bicarbonate species would show up at 1630 cm^{-1}, if exists (Davis

This is a preprint, the final version is subject to change, of the American Mineralogist (MSA)
Cite as Authors (Year) Title. American Mineralogist, in press.
(DOI will not work until issue is live.) DOI: http://dx.doi.org/10.2138/am-2016-5563

Oliver, 1972; Wen and Brooker, 1995). The Raman spectra for the fluid inclusion in the carbon-bearing enstatite do not show the peak due to carbonate species. Therefore the carbonate peak observed in the ^{13}C NMR is not from the inclusion. In order to check the potential presence of carbonate phases in the grains, we also performed SEM analysis of the grains. The preliminary analysis does not show any evidence for the carbonate phases although we cannot discard the possibility of its potential presence (See appendix A5 and A6).

Sources of ^{12}C contamination

In this study, ^{13}C-enriched amorphous carbon (~ 99.7%) was used to synthesize the carbon-bearing enstatite and the sample was sealed in a Pt tube (a closed system); therefore, the presence of ^{12}C was not expected. The Raman spectra for fluid-inclusion in enstatite, however, showed the presence of ^{12}C species, which was not present inside the capsule during the sample preparation and welding. The presence of ^{12}C thus indicates a potential contamination by infiltration of carbon from the graphite furnace during the compression and heating in the piston cylinder (Balta et al., 2011; Brooker et al., 1998; Brooker et al., 1999; Ni and Keppler, 2013). Note that double Pt capsules were used to minimize the changes in f_{O2} in several previous synthesis of carbon-bearing silicates in the previous studies (Balta et al., 2011; Brooker et al., 1998; Ni and Keppler, 2013 and references therein). The ^{12}C infiltrated from the graphite furnace may lead to the spatial heterogeneity in f_{O2}: oxygen fugacity near the boundary of the Pt capsule may be low, resulting in the formation of ^{13}CO species [*via* $^{13}CO_2 + {}^{12}C$ (from graphite furnace) $= {}^{13}CO + {}^{12}CO$] (Brooker et al., 1998; Cerfontain et al., 1987). Despite the observed presence of ^{12}C in the carbon-bearing enstatite (Fig. 1), the ^{13}C MAS NMR spectrum obtained from the sample shows only the ^{13}C contribution in enstatite, taking into consideration the fact that the ^{13}C

This is a preprint, the final version is subject to change, of the American Mineralogist (MSA)
Cite as Authors (Year) Title. American Mineralogist, in press.
(DOI will not work until issue is live.) DOI: http://dx.doi.org/10.2138/am-2016-5563

563 is the only active isotope.

564

565 ## IMPLICATIONS

566 Here, we have reported the ^{13}C MAS NMR spectrum for carbon-bearing enstatite. The
567 ^{13}C MAS NMR spectrum for the carbon-bearing enstatite shows multiple peaks from different
568 carbon environments: CO, CO_3^{2-}, and molecular CO_2. The Raman spectra for the observed fluid
569 inclusion in the carbon-bearing enstatite show multiple molecular species (e.g., CO_2, CO, CH_4,
570 H_2O, and H_2). The quantum chemical calculations of the $C(OH)_4$ cluster show that ^{13}C chemical
571 shift of the cluster has strong C-O bond length dependence; with increasing C-O bond length
572 from 1.40 Å to 1.60 Å, ^{13}C chemical shift increases from 121.2 ppm to 196.9 ppm.

573 While the Raman spectrum of the observed fluid inclusions in the carbon-bearing
574 enstatite can provide information on the collective vibration of molecules of different isotopes
575 (e.g., peaks of $^{13}CO_2$ and $^{12}CO_2$, and ^{13}CO and ^{12}CO), the ^{13}C NMR spectrum can provide
576 complementary and element-specific information on the nature of carbon species in crystalline
577 silicates, distinguishing the molecular CO_2 in fluid phase and structurally bound CO_2 in silicate
578 network. Taking into consideration the similarity between the chemical shifts of CO_2 and $^{[4]}C$, it
579 is not straightforward to assign the peak solely based on the ^{13}C NMR peak positions. Yet, we
580 expect that the method could potentially probe the minor fraction of $^{[4]}C$ whose peak width is
581 expected to be much larger than that of molecular CO_2 due to its pronounced nuclear spin
582 anisotropy. The current results suggest that the ^{13}C MAS NMR technique, combined with Raman
583 spectroscopy can be used as a tool for the detection of carbon species and inclusions in
584 crystalline silicates.

585 Whereas the ^{13}C MAS NMR technique was utilized to probe carbon speciation in

This is a preprint, the final version is subject to change, of the American Mineralogist (MSA)
Cite as Authors (Year) Title. American Mineralogist, in press.
(DOI will not work until issue is live.) DOI: http://dx.doi.org/10.2138/am-2016-5563

586 silicates at relatively low pressure (1.5 GPa in the current study), the method can also be utilized
587 to analyze carbon species in carbon-bearing silicate minerals at much higher pressure and
588 additional carbon reservoirs in earth's interior, such as metal carbides and carbonate minerals
589 (Catalli and Williams, 2005; Hazen et al., 2013; Mikhail et al., 2011; Mookherjee, 2011;
590 Mookherjee et al., 2011; Oganov et al., 2013; Rohrbach and Schmidt, 2011; Santillán et al., 2005;
591 Seto et al., 2008). As for the latter, presence of crystalline silicon carbonate phase where silicon
592 behaves as a metal cation in carbonates at 18–26 GPa was also reported (Santoro et al., 2011).
593 While the detailed structural characterization of these phases remains to be seen, future ^{13}C solid-
594 state NMR studies of these phases may reveal the detailed bonding nature of these complexes
595 under compression.

596 The solubility of carbon into $(Mg,Fe)_2SiO_4$ olivine increases from 0.09 ppm to 12.75 ppm
597 as pressure increases from 1.5 GPa to 11 GPa and that into $MgSiO_3$ bridgmanite at ~ 26 GPa is
598 less than 0.05 ppm (Shcheka et al., 2006). Due to relatively low carbon solubility, it is currently
599 challenging to detect carbon species in these phases using the experimental conditions employed
600 here. While the NMR data indeed provide complementary and unique insights into the speciation
601 of carbon-bearing phases to vibrational spectroscopy, we fully acknowledged the fact that the
602 current data also address the limitation of the NMR studies on quantitative estimation of ~ ppm
603 scales of carbon dissolved in a crystalline lattice: ^{13}C may not reveal the carbon species at
604 concentration below 5–10 ppm using the current experimental protocols at the current stage.
605 NMR experiments at high magnetic field with fast spinning probes lead to significant gain in
606 signal intensity and may provide insights into the carbon solubility mechanism into the
607 crystalline phases in Earth's mantle.

608

This is a preprint, the final version is subject to change, of the American Mineralogist (MSA)
Cite as Authors (Year) Title. American Mineralogist, in press.
(DOI will not work until issue is live.) DOI: http://dx.doi.org/10.2138/am-2016-5563

ACKNOWLEDGEMENT

This research was supported by National Research Foundation, Korea Laboratory Program to S.K.L. (2014-053-046). We thank I. Lee (SNU), C.S. Yoo (WSU), G.D. Cody (CIW) for helpful discussions, B. Phillips (SUNY, Stony Brook) for constructive suggestions, which greatly improved quality and clarify of the manuscript, and three anonymous reviewers and Y. Morizet for helpful comments and suggestions on the original manuscript.

615 ## REFERENCES CITED

616 Abou-Hamad, E., Babaa, M.R., Bouhrara, M., Kim, Y., Saih, Y., Dennler, S., Mauri, F., Basset,
617 J.M., Goze-Bac, C., and Wågberg, T. (2011) Structural properties of carbon nanotubes
618 derived from ^{13}C NMR. Physical Review B, 84, 165417
619 Alam, T.M., Friedmann, T.A., and Jurewicz, J.G. (2002) Solid state ^{13}C MAS NMR
620 investigations of amorphous carbon thin films structural changes during annealing. In J.S.
621 M. P. Soriaga, L. A. Bottomley and Y.-G. Kim, Ed. Thin Films: Preparation,
622 Characterization, Applications, p. 277-289. Kluwer, New York
623 Alam, T.M., Friedmann, T.A., Schultz, P.A., and Sebastiani, D. (2003) Low temperature
624 annealing in tetrahedral amorphous carbon thin films observed by ^{13}C NMR spectroscopy.
625 Physical Review B, 67, 245309
626 Balta, J.B., Asimow, P.D., and Mosenfelder, J.L. (2011) Hydrous, low-carbon melting of garnet
627 peridotite. Journal of Petrology, 52, 2079-2105
628 Blank, J.G., and Brooker, R.A. (1994) Experimental studies of carbon dioxide in silicate melts:
629 Solubility, speciation, and stable carbon isotope behavior. In M.R. Carroll, and J.R.
630 Holloway, Eds. Reviews in Mineralogy and Geochemistry, 30, p. 157-186. Mineralogical
631 Society of America, Washington
632 Blank, J.G., Stolper, E.M., and Carroll, M.R. (1993) Solubilities of caron-dioxide and water in
633 rhyolitic melt at 850 °C and 750 bars. Earth and Planetary Science Letters, 119, 27-36
634 Blundy, J., Cashman, K.V., Rust, A., and Witham, F. (2010) A case for CO_2-rich arc magmas.
635 Earth and Planetary Science Letters, 290, 289-301
636 Bodnar, R.J., Binns, P.R., and Hall, D.L. (1989) Synthetic fluid inclusions - VI. Quantitative
637 evaluation of the decrepitation behaviour of fluid inclusions in quartz at one atmosphere

638 confining pressure. Journal of Metamorphic Geology, 7, 229-242
639 Brooker, R., Holloway, J.R., and Hervig, R. (1998) Reduction in piston-cylinder experiments:
640 The detection of carbon infiltration into platinum capsules. American Mineralogist, 83, 985-
641 994
642 Brooker, R.A., Kohn, S.C., Holloway, J.R., McMillan, P.F., and Carroll, M.R. (1999) Solubility,
643 speciation and dissolution mechanisms for CO_2 in melts on the $NaAlO_2$-SiO_2 join.
644 Geochimica et Cosmochimica Acta, 63, 3549-3565
645 Burke, E.A.J. (2001) Raman microspectrometry of fluid inclusions. Lithos, 55, 139-158
646 Burton, M.R., Sawyer, G.M., and Granieri, D. (2013) Deep carbon emissions from volcanoes. In
647 R.M. Hazen, A.P. Jones, and J.A. Baross, Eds. Reviews in Mineralogy & Geochemistry, 75,
648 p. 323-354. Mineralogial Society of America, Virginia
649 Catalli, K., and Williams, Q. (2005) A high-pressure phase transition of calcite-III. American
650 Mineralogist, 90, 1679-1682
651 Cerfontain, M.B., Meijer, R., Kapteijn, F., and Moulijn, J.A. (1987) Alkali-catalyzed carbon
652 gasification in CO-CO_2 mixtures: An extended model for the oxygen exchange and
653 gasification reaction. Journal of Catalysis, 107, 173-180
654 Cho, G., Yen, B.K., and Klug, C.A. (2008) Structural characterization of sputtered hydrogenated
655 amorphous carbon films by solid state nuclear magnetic resonance. Journal of Applied
656 Physics, 104, 013531
657 Cody, G.D., and Alexander, C.M.O.D. (2005) NMR studies of chemical structural variation of
658 insoluble organic matter from different carbonaceous chondrite groups. Geochimica et
659 Cosmochimica Acta, 69, 1085-1097
660 Cody, G.D., Heying, E., Alexander, C.M.O., Nittler, L.R., Kilcoyne, A.L.D., Sandford, S.A., and

661 Stroud, R.M. (2011) Establishing a molecular relationship between chondritic and cometary
662 organic solids. Proceedings of the National Academy of Sciences of the United States of
663 America, 108, 19171-19176
664 Davis, A.R., and Oliver, B.G. (1972) A vibrational-spectroscopic study of the species present in
665 the CO_2−H_2O system. Journal of Solution Chemistry, 1, 329-339
666 Dixon, J.E., and Clague, D.A. (2001) Volatiles in basaltic glasses from Loihi seamount, Hawaii:
667 Evidence for a relatively dry plume component. Journal of Petrology, 42, 627-654
668 Eggler, D.H., and Kadik, A.A. (1979) System $NaAlSi_3O_8$-H_2O-CO_2 to 20 kbar pressure: 1.
669 Compositional and thermodynamic relations of liquids and vapors coexisting with albite.
670 American Mineralogist, 64, 1036-1048
671 Eggler, D.H., and Rosenhauer, M. (1978) Carbon-dioxide in silicate melts: 2. Solubilites of CO_2
672 and H_2O in $CaMgSi_2O_6$ (diopside) liquids and vapors at pressure to 40 kb. American
673 Journal of Science, 278, 64-94
674 Etesse, P., Zega, J.A., and Kobayashi, R. (1992) High pressure nuclear magnetic resonance
675 measurement of spin–lattice relaxation and self-diffusion in carbon dioxide. Journal of
676 Chemical Physics, 97, 2022
677 Ettinger, R., Blume, P., Patterson, A., and Lauterbur, P.C. (1960) ^{13}C chemical shifts in CO and
678 CO_2. Journal of Chemical Physics, 33, 1597-1598
679 Feng, J., Lee, Y.J., Reeder, R.J., and Phillips, B.L. (2006) Observation of bicarbonate in calcite
680 by NMR spectroscopy. American Mineralogist, 91, 957-960
681 Fine, G., and Stolper, E. (1985) The speciation of carbon-dioxide in sodium aluminosilicate
682 glasses. Contributions to Mineralogy and Petrology, 91, 105-121
683 Freund, F. (1981) Mechanism of the water and carbon dioxide solubility in oxides and silicates

and the role of O^-. Contributions to Mineralogy and Petrology, 76, 474-482

Freund, F., Kathrein, H., Wengeler, H., Knobel, R., and Reinen, H.J. (1980) Carbon in solid solution in forsterite--a key to the untractable nature of reduced carbon in terrestrial and cosmogenic rocks. Geochimica et Cosmochimica Acta, 44, 1319-1321, 1323-1333

Frisch, M.J., and others. (2004) Gaussian 03, Revision C.02. Gaussian, Inc., Wallingford CT

Fyfe, W.S. (1970) Lattice energies, phase transformations and volatiles in the mantle. Physics of the Earth and Planetary Interiors, 3, 196-200

Garrabos, Y., Echargui, M.A., and Marsault-Herail, F. (1989) Comparison between the density effects on the levels of the Raman spectra of the Fermi resonance doublet of the $^{12}C^{16}O_2$ and $^{13}C^{16}O_2$ molecules. The Journal of Chemical Physics, 91, 5869-5881

Gerlach, T.M., McGee, K.A., Elias, T., Sutton, A.J., and Doukas, M.P. (2002) Carbon dioxide emission rate of Kīlauea Volcano: Implications for primary magma and the summit reservoir. Journal of Geophysical Research: Solid Earth, 107, 2189

Green, H.W. (1972) A CO_2 charged asthenosphere. Nature Physical Science, 238, 2-5

Hazen, R.M., Downs, R.T., Jones, A.P., and Kah, L. (2013) Carbon mineralogy and crystal chemistry. In R.M. Hazen, A.P. Jones, and J.A. Baross, Eds. Reviews in Mineralogy and Geochemistry, 75, p. 7-46. Mineralogical Society of America, Virginia

Herzfeld, J., and Berger, A.E. (1980) Sideband intensities in NMR spectra of samples spinning at the magic angle. The Journal of Chemical Physics, 73, 6021-6030

Jäger, C., Henning, T., Schlögl, R., and Spillecke, O. (1999) Spectral properties of carbon black. Journal of Non-Crystalline Solids, 258, 161-179

Jambon, A. (1994) Earth degassing and large-scale geochemical cycling of volatile elements. In M.R. Carroll, and J.R. Holloway, Eds. Reviews in Mineralogy and Geochemistry, 30, p.

479-517. Mineralogical Society of America, Washington

Jones, A.R., Winter, R., Greaves, G.N., and Smith, I.H. (2005) ^{23}Na, ^{29}Si, and ^{13}C MAS NMR investigation of glass-forming reactions between Na_2CO_3 and SiO_2. Journal of Physical Chemistry B, 109, 23154-23161

Kadik, A., Pineau, F., Litvin, Y., Jendrzejewski, N., Martinez, I., and Javoy, M. (2004) Formation of carbon and hydrogen species in magmas at low oxygen fugacity. Journal of Petrology, 45, 1297-1310

Kaminski, É., and Jaupart, C. (1997) Expansion and quenching of vesicular magma fragments in Plinian eruptions. Journal of Geophysical Research: Solid Earth, 102, 12187-12203

Kanowski, M., Vieth, H.M., Lüders, K., Buntkowsky, G., Belz, T., Werner, H., Wohlers, M., and Schlögl, R. (1997) The structure of fullerene black and the incorporation of C_{60} investigated by ^{13}C NMR. Carbon, 35, 685-695

Keppler, H., Wiedenbeck, M., and Shcheka, S.S. (2003) Carbon solubility in olivine and the mode of carbon storage in the Earth's mantle. Nature, 424, 414-416

Kim, E.J., and Lee, S.K. (2011) Atomic structure of dissolved carbon in enstatite: Raman spectroscopy and quantum chemical calculations of NMR chemical shift. Journal of Mineralogical Society of Korea, 24, 289-300 (in Korean).

Kirkpatrick, R.J., and Brow, R.K. (1995) Nuclear-magnetic-resonance investigation of the structures of phosphate and phospahte-containing glasses: A review. Solid State Nuclear Magnetic Resonance, 5, 9-21

Kirkpatrick, R.J., Oestrike, R., Weiss, C.A., Smith, K.A., and Oldfield, E. (1986) High-resolution ^{27}Al and ^{29}Si NMR spectroscopy of glasses and crystals along the join $CaMgSi_2O_6$-$CaAl_2SiO_6$. American Mineralogist, 71, 705-711

730 Kobayashi, T., Yamamoto, J., Hirajima, T., Ishibashi, H., Hirano, N., Lai, Y., Prikhod'ko, V.S.,
731 and Arai, S. (2012) Conformity and precision of CO_2 densimetry in CO_2 inclusions:
732 Microthermometry versus Raman microspectroscopic densimetry. Journal of Raman
733 Spectroscopy, 43, 1126-1133
734 Kohn, S.C., Brooker, R.A., and Dupree, R. (1991) ^{13}C MAS NMR: A method for studying CO_2
735 speciation in glasses. Geochimica et Cosmochimica Acta, 55, 3879-3884
736 Kwak, J.H., Hu, J.Z., Hoyt, D.W., Sears, J.A., Wang, C.M., Rosso, K.M., and Felmy, A.R. (2010)
737 Metal carbonation of forsterite in supercritical CO_2 and H_2O using solid state ^{29}Si, ^{13}C NMR
738 spectroscopy. Journal of Physical Chemistry C, 114, 4126-4134
739 Lee, B.H., and Lee, S.K. (2009) Effect of lattice topology on the adsorption of benzyl alcohol on
740 kaolinite surfaces: Quantum chemical calculations of geometry optimization, binding
741 energy, and NMR chemical shielding. American Mineralogist, 94, 1392-1404
742 Lee, S.K. (2010) Effect of pressure on structure of oxide glasses at high pressure: Insights from
743 solid-state NMR of quadrupolar nuclides. Solid State Nuclear Magnetic Resonance, 38, 45-
744 57
745 -. (2011) Simplicity in melt densification in multicomponent magmatic reservoris in Earth's
746 interior revealed by multinuclear magnetic resonance. Proceedings of the National Academy
747 of Sciences of the United States of America, 108, 6847-6852
748 Lee, S.K., and Ahn, C.W. (2014) Probing of 2 dimensional confinement-induced structural
749 transitions in amorphous oxide thin film. Scientific reports, 4, 4200
750 Lee, S.K., Cody, G.D., Fei, Y.W., and Mysen, B.O. (2004) Nature of polymerization and
751 properties of silicate melts and glasses at high pressure. Geochimica et Cosmochimica Acta,
752 68, 4189-4200

753 Lee, S.K., Lee, S.B., Park, S.Y., Yi, Y.S., and Ahn, C.W. (2009) Structure of amorphous
754 aluminum oxide. Physical Review Letters, 103
755 Lee, S.K., Park, S.Y., Yi, Y.S., and Moon, J. (2010) Structure and disorder in amorphous alumina
756 thin films: Insights from high-resolution solid-state NMR. The Journal of Physical
757 Chemistry C, 114, 13890-13894
758 Lee, S.K., Yi, Y.S., Cody, G.D., Mibe, K., Fei, Y., and Mysen, B.O. (2012) Effect of network
759 polymerization on the pressure-induced structural changes in sodium aluminosilicate
760 glasses and melts: ^{27}Al and ^{17}O solid-state NMR study. The Journal of Physical Chemistry C,
761 116, 2183-2191
762 Lin, F., Bodnar, R.J., and Becker, S.P. (2007) Experimental determination of the Raman CH_4
763 symmetric stretching (ν_1) band position from 1–650 bar and 0.3–22°C: Application to fluid
764 inclusion studies. Geochimica et Cosmochimica Acta, 71, 3746-3756
765 Lin, Y., Zhang, L., Mao, H.-k., Chow, P., Xiao, Y., Baldini, M., Shu, J., and Mao, W.L. (2011)
766 Amorphous diamond: A high-pressure superhard carbon allotrope. Physical Review Letters,
767 107
768 Lloyd, A.S., Ruprecht, P., Hauri, E.H., Rose, W., Gonnermann, H.M., and Plank, T. (2014)
769 NanoSIMS results from olivine-hosted melt embayments: Magma ascent rate during
770 explosive basaltic eruptions. Journal of Volcanology and Geothermal Research, 283, 1-18
771 Mathez, E.A., Dietrich, V.J., and Irving, A.J. (1984) The geochemistry of carbon in mantle
772 peridotites. Geochimica et Cosmochimica Acta, 48, 1849-1859
773 Mikhail, S., Shahar, A., Hunt, S.A., Jones, A.P., and Verchovsky, A.B. (2011) An experimental
774 investigation of the pressure effect on stable isotope fractionation at high temperature:
775 Implications for mantle processes and core formation in celestial bodies from 1 GPa and up

776 to 25 GPa. 42nd Lunar and Planetary Science Conference, The Woodlands, Texas
777 Mookherjee, M. (2011) Elasticity and anisotropy of Fe_3C at high pressures. American
778 Mineralogist, 96, 1530-1536
779 Mookherjee, M., Nakajima, Y., Steinle-Neumann, G., Glazyrin, K., Wu, X., Dubrovinsky, L.,
780 McCammon, C., and Chumakov, A. (2011) High-pressure behavior of iron carbide (Fe_7C_3)
781 at inner core conditions. Journal of Geophysical Research: Solid Earth, 116, B04201
782 Moore, J.K., Surface, J.A., Brenner, A., Skemer, P., Conradi, M.S., and Hayes, S.E. (2015)
783 Quantitative identification of metastable magnesium carbonate minerals by solid-state ^{13}C
784 NMR spectroscopy. Environmental Science & Technology, 49, 657-664
785 Morizet, Y., Brooker, R.A., and Kohn, S.C. (2002) CO_2 in haplo-phonolite melt: Solubility,
786 speciation and carbonate complexation. Geochimica et Cosmochimica Acta, 66, 1809-1820
787 Morizet, Y., Paris, M., Gaillard, F., and Scaillet, B. (2009) Raman quantification factor
788 calibration for CO-CO_2 gas mixture in synthetic fluid inclusions: Application to oxygen
789 fugacity calculation in magmatic systems. Chemical Geology, 264, 58-70
790 -. (2010) C-O-H fluid solubility in haplobasalt under reducing conditions: An experimental study.
791 Chemical Geology, 279, 1-16
792 Mysen, B. (2013) Structure–property relationships of COHN-saturated silicate melt coexisting
793 with COHN fluid: A review of in-situ, high-temperature, high-pressure experiments.
794 Chemical Geology, 346, 113-124
795 Mysen, B.O., Arculus, R.J., and Eggler, D.H. (1975) Solubility of carbon-dioxide in melts of
796 andesite, tholeiite, and olivine nephelinite composition to 30 kbar pressure. Contributions to
797 Mineralogy and Petrology, 53, 227-239
798 Mysen, B.O., Fogel, M.L., Morrill, P.L., and Cody, G.D. (2009) Solution behavior of reduced C-

O-H volatiles in silicate melts at high pressure and temperature. Geochimica et Cosmochimica Acta, 73, 1696-1710

Mysen, B.O., Kumamoto, K., Cody, G.D., and Fogel, M.L. (2011) Solubility and solution mechanisms of C–O–H volatiles in silicate melt with variable redox conditions and melt composition at upper mantle temperatures and pressures. Geochimica et Cosmochimica Acta, 75, 6183-6199

Mysen, B.O., and Richet, P. (2005) Volatiles I. The system C-O-H-S. Silicate Glasses and Melts, 10. Elsevier

Ni, H.W., and Keppler, H. (2013) Carbon in silicate melts. In R.M. Hazen, A.P. Jones, and J.A. Baross, Eds. Reviews in Mineralogy and Geochemistry, 75, p. 251-287. Mineralogical Society of America, Virginia

Oganov, A.R., Hemley, R.J., Hazen, R.M., and Jones, A.P. (2013) Structure, bonding, and mineralogy of carbon at extreme conditions. In R.M. Hazen, A.P. Jones, and J.A. Baross, Eds. Reviews in Mineralogy and Geochemistry, 75, p. 47-77. Mineralogical Society of America, Virginia

Pan, H., Pruski, M., Gerstein, B.C., Li, F., and Lannin, J.S. (1991) Local coordination of carbon atoms in amorphous carbon. Physical Review B, 44, 6741-6745

Papenguth, H.W., Kirkpatrick, R.J., Montez, B., and Sandberg, P.A. (1989) ^{13}C MAS NMR spectroscopy of inorganic and biogenic carbonates. American Mineralogist, 74, 1152-1158

Parfitt, E.A., and Wilson, L. (2008) The role of volatiles. Fundamentals of Physical Volcanology, p. 64-76. Blackwell Science

Pawley, A.R., Holloway, J.R., and McMillan, P.F. (1992) The effect of oxygen fugacity on the solubility of carbon oxygen fluids in basaltic melt. Earth and Planetary Science Letters, 110,

213-225

Phillips, B.L., Xu, H., Heaney, P.J., and Navrotsky, A. (2000) ^{29}Si and ^{27}Al MAS-NMR spectroscopy of β-eucryptite ($LiAlSiO_4$): The enthalpy of Si,Al ordering. American Mineralogist, 85, 181-188

Pretsch, E., Buhlmann, P., and Badertscher, M. (2009) Structure Determination of Organic Compounds - Tables of Spectral Data. Springer, Berlin

Resing, H.A. (1969) NMR relaxation in adamantane and hexamethylenetetramine: Diffusion and rotation. Molecular Crystals, 9, 101-132

Richet, P., and Bottinga, Y. (1984) Anorthite, andesine, wollastonite, diopside, cordierite, and pyrope: Thermodynamics of melting, glass transitions, and properties of the amorphous phases. Earth and Planetary Science Letters, 67, 415-432

Rockafellow, E.M., Fang, X., Trewyn, B.G., Schmidt-Rohr, K., and Jenks, W.S. (2009) Solid-state ^{13}C NMR characterization of carbon-modified TiO_2. Chemistry of Materials: A Publication of the American Chemical Society, 21, 1187-1197

Rohrbach, A., and Schmidt, M.W. (2011) Redox freezing and melting in the Earth's deep mantle resulting from carbon-iron redox coupling. Nature, 472, 209-212

Rosso, K.M., and Bodnar, R.J. (1995) Microthermometric and Raman spectroscopic detection limits of CO_2 in fluid inclusions and the Raman spectroscopic characterization of CO_2. Geochimica et Cosmochimica Acta, 59, 3961-3975

Rust, A.C., and Cashman, K.V. (2011) Permeability controls on expansion and size distributions of pyroclasts. Journal of Geophysical Research: Solid Earth, 116, B11202

Santillán, J., Catalli, K., and Williams, Q. (2005) An infrared study of carbon-oxygen bonding in magnesite to 60 GPa. American Mineralogist, 90, 1669-1673

Santoro, M., Gorelli, F., Haines, J., Cambon, O., Levelut, C., and Garbarino, G. (2011) Silicon carbonate phase formed from carbon dioxide and silica under pressure. Proceedings of the National Academy of Sciences of the United States of America, 108, 7689-7692

Seitz, J.C., Pasteris, J.D., and Chou, I. (1996) Raman spectrscopic characterization of gas mixtures. II quantitative composition and pressure determination of the CO_2-CH_4 system. American Journal of Science, 296, 577-600

Sen, S., Widgeon, S.J., Navrotsky, A., Mera, G., Tavakoli, A., Ionescu, E., and Riedel, R. (2013) Carbon substitution for oxygen in silicates in planetary interiors. Proceedings of the National Academy of Sciences, 110, 15904-15907

Seto, Y., Hamane, D., Nagai, T., and Fujino, K. (2008) Fate of carbonates within oceanic plates subducted to the lower mantle, and a possible mechanism of diamond formation. Physics and Chemistry of Minerals, 35, 223-229

Shcheka, S.S., Wiedenbeck, M., Frost, D.J., and Keppler, H. (2006) Carbon solubility in mantle minerals. Earth and Planetary Science Letters, 245, 730-742

Shindo, K., Kondo, T., and Sakurai, Y. (2011) ^{1}H NMR study of hydrogen stored in activated carbon powder prepared by mechanical milling. Journal of Alloys and Compounds, 509, 4534-4537

Si, Y., and Samulski, E.T. (2008) Synthesis of water soluble graphene. Nano Letters, 8, 1679-1682

Sides, I., Edmonds, M., Maclennan, J., Houghton, B.F., Swanson, D.A., and Steele-MacInnis, M.J. (2014) Magma mixing and high fountaining during the 1959 Kīlauea Iki eruption, Hawai‘i. Earth and Planetary Science Letters, 400, 102-112

Stebbins, J.F. (1995) Dynamics and structure of silicate and oxide melts: Nuclear magnetic

resonance studies. Structure, Dynamics and Properties of Silicate Melts, 32, 191-246

Stebbins, J.F., and Xue, X. (2014) NMR spectroscopy of inorganic Earth materials. In G.S. Henderson, D.R. Neuville, and R.T. Downs, Eds. Reviews in Mineralogy and Geochemistry, 78, p. 605-653. Mineralogical Society of America, Virginia

Stolper, E., Fine, G., Johnson, T., and Newman, S. (1987) Solubility of carbon dioxide in albitic melt. American Mineralogist, 72, 1071-1085

Sugioka, I., and Bursik, M. (1995) Explosive fragmentation of erupting magma. Nature, 373, 689-692

Tangeman, J.A., Phillips, B.L., Navrotsky, A., Weber, J.K.R., Hixson, A.D., and Key, T.S. (2001) Vitreous forsterite (Mg_2SiO_4): Synthesis, structure, and thermochemistry. Geophysical Research Letters, 28, 2517-2520

Taylor, R., Hare, J.P., Abdul-Sada, A.K., and Kroto, H.W. (1990) Isolation, separation and characterisation of the fullerens C_{60} and C_{70}: The third form of carbon. Journal of Chemistry Society, Chemical Communications, 1423-1425

Tingle, T.N., and Aines, R.D. (1988) Beta-track autoradiography and infrared-spectroscopy bearing on the solubility of CO_2 in albite melt at 2 GPa and 1450 °C. Contributions to Mineralogy and Petrology, 100, 222-225

Tossell, J.A. (1995) Calculation of the ^{13}C NMR shieldings of the CO_2 complexes of aluminosilicates. Geochimica et Cosmochimica Acta, 59, 1299-1305

Tsong, I.S.T., and Knipping, U. (1986) Solute carbon and carbon segregation in magnesium-oxide signle-crystals - A secondary ion mass-spectrometry study - comment. Physics and Chemistry of Minerals, 13, 277-279

Tsong, I.S.T., Knipping, U., Loxton, C.M., Magee, C.W., and Arnold, G.W. (1985) Carbon on

surfaces of magnesium oxide and olivine single crystals. Diffusion from the bulk or surface contamination? Physics and Chemistry of Minerals, 12, 261-270

Wallace, P.J. (2005) Volatiles in subduction zone magmas: concentrations and fluxes based on melt inclusion and volcanic gas data. Journal of Volcanology and Geothermal Research, 140, 217-240

Wen, N., and Brooker, M.H. (1995) Ammonium carbonate, ammonium bicarbonate, and ammonium carbamate equilibria: A Raman study. The Journal of Physical Chemistry, 99, 359-368

Wright, R.B., and Wang, C.H. (1973) Density effect on the Fermi resonance in gaseous CO_2 by Raman scattering. The Journal of Chemical Physics, 58, 2893-2895

Zhang, C., and Duan, Z.H. (2010) GFluid: An Excel spreadsheet for investigating C-O-H fluid composition under high temperatures and pressures. Computers & Geosciences, 36, 569-572

Zhang, Y., and Zindler, A. (1993) Distribution and evolution of carbon and nitrogen in Earth. Earth and Planetary Science Letters, 117, 331-345

908 **Figure captions.**

909 **Figure 1|** (A) A stereoscopic micrograph image of one of the grains of carbon-bearing enstatite.
910 The size of the grain is 80 μm (w) × 100 μm (h) and the fluid inclusions are 4 μm (w) × 10
911 μm (h) (indicated with red rectangles). (B) Raman spectra for carbon-bearing enstatite in the
912 frequency range of 1000–4300 cm^{-1} and (C) that in the range of 1200–1500 cm^{-1} and (D)
913 2000–2200 cm^{-1}.

914 **Figure 2|** ^{13}C MAS NMR spectra for background-subtracted carbon-bearing enstatite (top),
915 carbon-bearing enstatite and stator and rotor backgrounds (middle), and stator and rotor
916 backgrounds (bottom). The asterisks denote expected positions of spinning sidebands for
917 125.2 ppm peak.

918 **Figure 3|** ^{13}C NMR spectra for carbon-bearing enstatite synthesized in this study (top) and
919 corresponding annealed sample at 750 °C for 10 min (bottom). All spectra were
920 background-subtracted.

921 **Figure 4|** ^{13}C NMR spectra for carbon-bearing enstatite and stator and rotor backgrounds at 11
922 kHz of spinning speed (top), that at 14 kHz of spinning speed (middle), and rotor and stator
923 background at 14 kHz (bottom). The asterisks and dotted arcs denote expected positions of
924 spinning side bands for background signal at 130 ppm. The spinning sideband of the
925 spectrum for carbon-bearing enstatite at 14 kHz overlaps with a small peak at ~ -9 ppm.

926 **Figure 5|** (A) Background-subtracted ^{13}C NMR spectra for ^{13}C-enriched compressed and
927 uncompressed amorphous carbon. (B) ^{13}C NMR spectra for ^{13}C-enriched uncompressed
928 amorphous carbon, and stator and rotor background. (C) ^{13}C NMR spectra for ^{13}C-enriched
929 compressed amorphous carbon, and stator and rotor background.

930 **Figure 6|** (A) Single point energy of $C(OH)_4$ cluster with varying C–O bond length. A model

931 $C(OH)_4$ cluster is also shown in the inset. (B) NMR chemical shift of $C(OH)_4$ cluster with
932 varying C–O bond length.

933 **Figure 7|** (Top) ^{13}C MAS NMR spectrum for the mixtures of ADM-SiO_2 with varying
934 ADM/SiO_2 ratio [X_{ADM} = 1/4 (25 wt%, 2750 ppm of ^{13}C), 1/8 (12.5 wt%, 1375 ppm of ^{13}C),
935 1/16 (6.25 wt%, 688 ppm of ^{13}C), 1/50 (2.0 wt%, 220 ppm of ^{13}C), 1/233 (0.43 wt%, 47
936 ppm of ^{13}C), 1/310 (0.32 wt%, 35 ppm of ^{13}C)]. (Bottom) Variation of peak intensity in the
937 ADM-SiO_2 mixture as a function of ^{13}C abundance (in ppm) calculated from nominal X_{ADM}
938 ratio and peak area of carbon species in ^{13}C MAS NMR spectra. Diamonds and circles refer
939 to the amounts of ^{13}C estimated from nominal X_{ADM} ratio with and without proton
940 decoupling, respectively. Their peak areas were retrieved from ^{13}C MAS NMR results for
941 ADM-SiO_2 mixtures. Rectangles refer to the amounts of ^{13}C species in carbon-bearing
942 enstatite estimated from ^{13}C MAS NMR spectra for carbon-bearing enstatite.
943
944

This is a preprint, the final version is subject to change, of the American Mineralogist (MSA)
Cite as Authors (Year) Title. American Mineralogist, in press.
(DOI will not work until issue is live.) DOI: http://dx.doi.org/10.2138/am-2016-5563

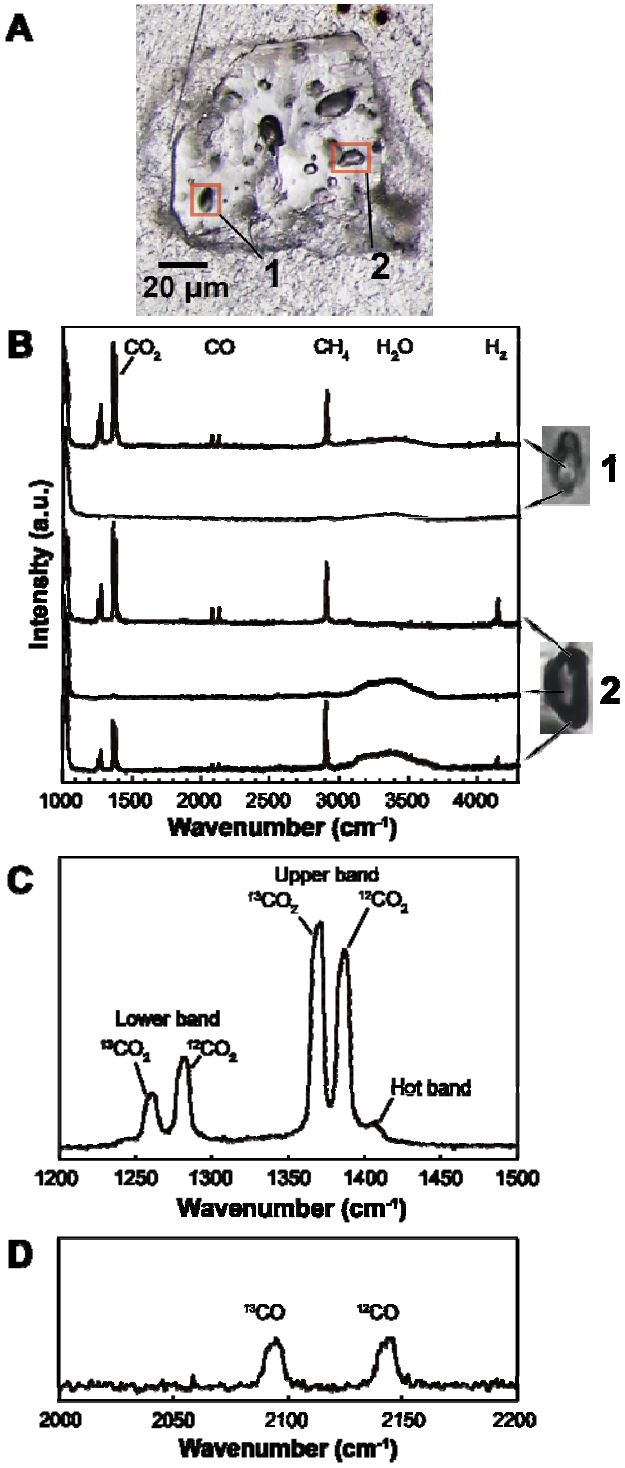

Figure 1.

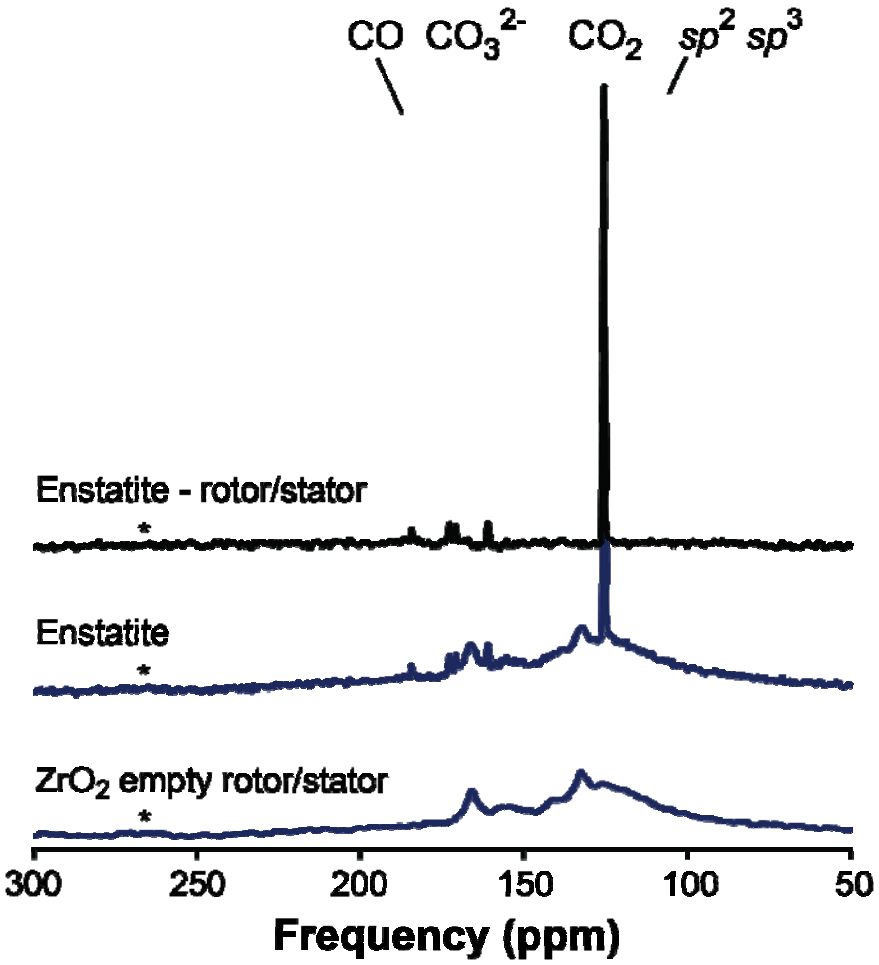

Figure 2.

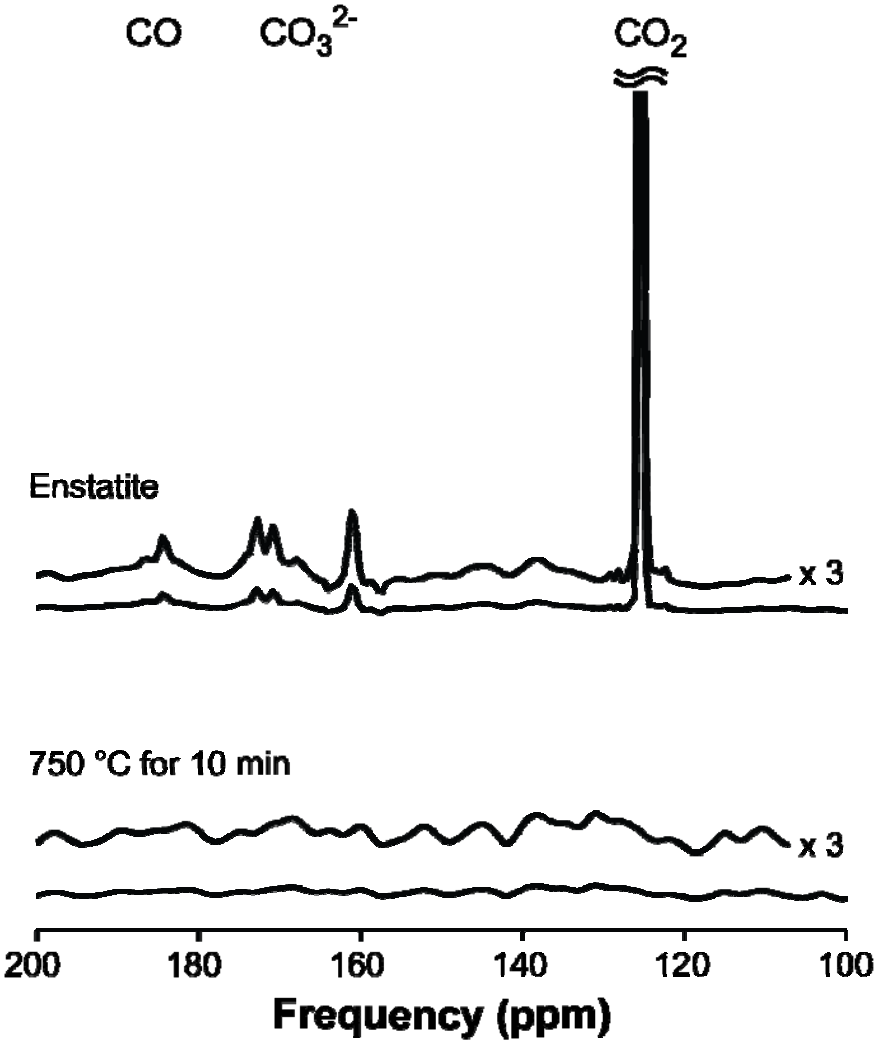

Figure 3.

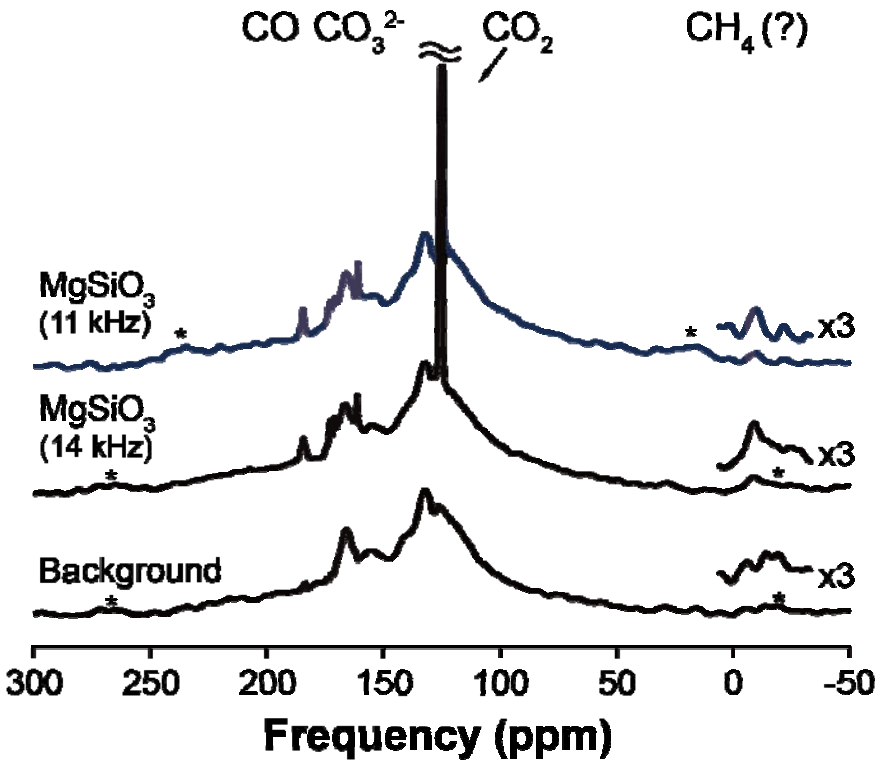

Figure 4.

This is a preprint, the final version is subject to change, of the American Mineralogist (MSA)
Cite as Authors (Year) Title. American Mineralogist, in press.
(DOI will not work until issue is live.) DOI: http://dx.doi.org/10.2138/am-2016-5563

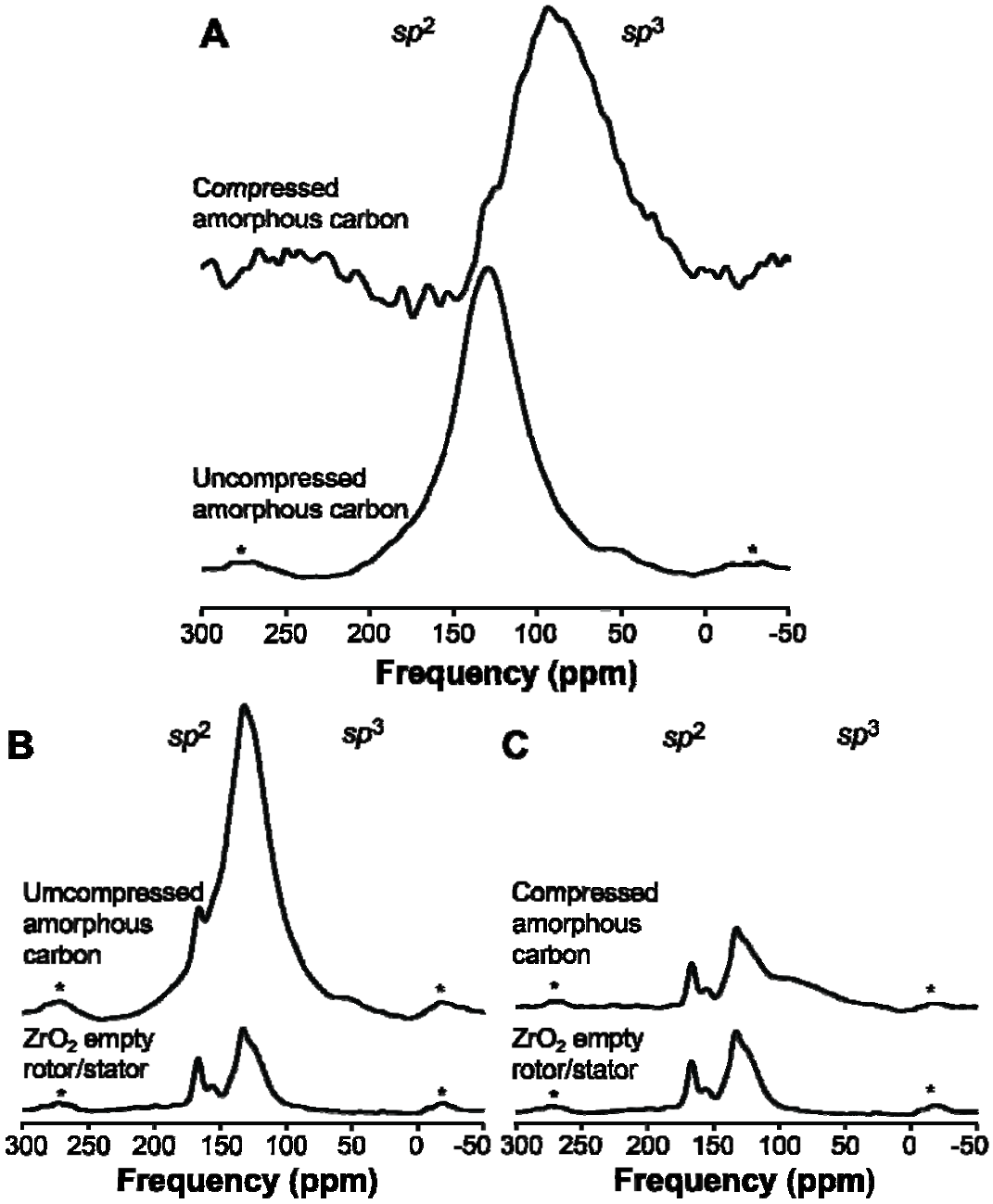

Figure 5.

This is a preprint, the final version is subject to change, of the American Mineralogist (MSA)
Cite as Authors (Year) Title. American Mineralogist, in press.
(DOI will not work until issue is live.) DOI: http://dx.doi.org/10.2138/am-2016-5563

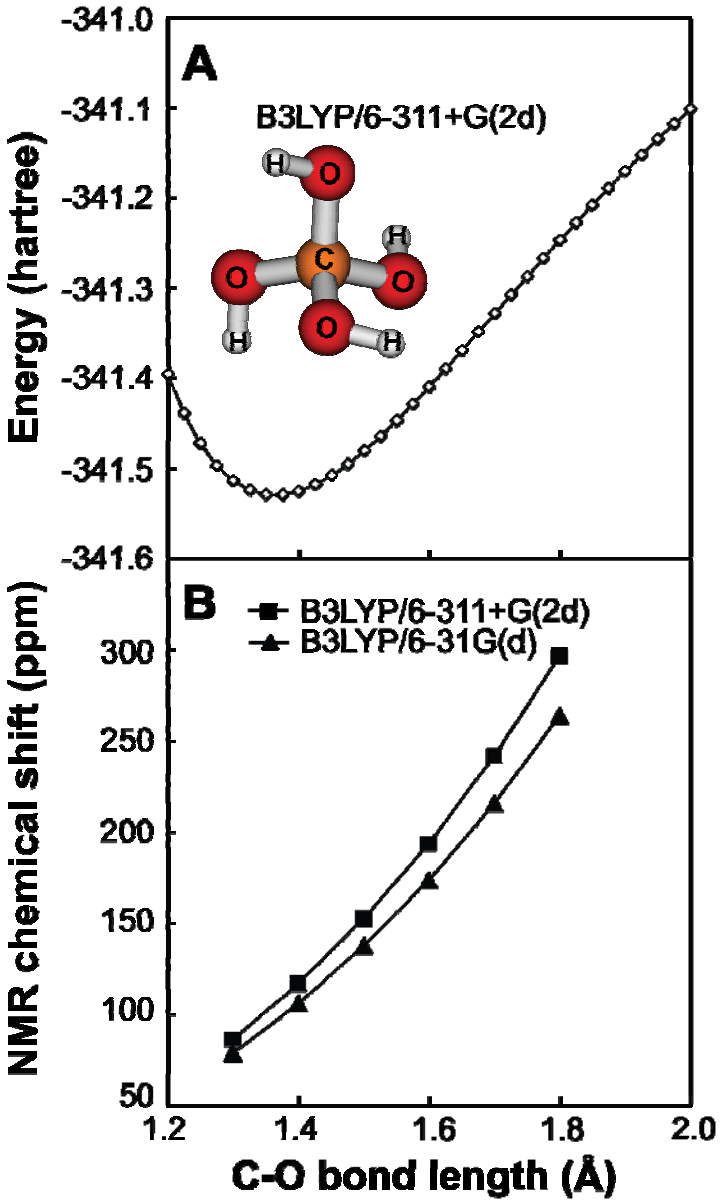

Figure 6.

This is a preprint, the final version is subject to change, of the American Mineralogist (MSA)
Cite as Authors (Year) Title. American Mineralogist, in press.
(DOI will not work until issue is live.) DOI: http://dx.doi.org/10.2138/am-2016-5563

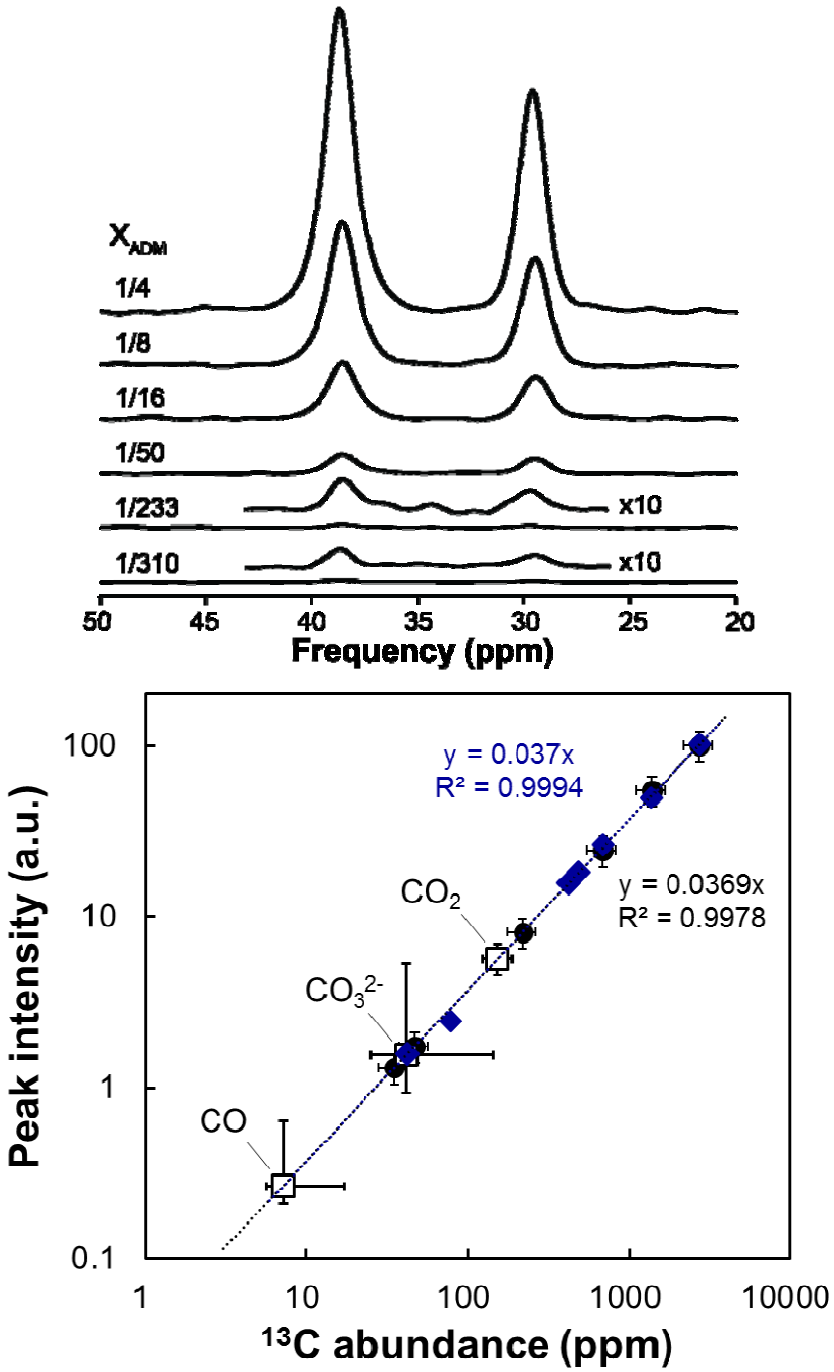

Figure 7.

1045

This is a preprint, the final version is subject to change, of the American Mineralogist (MSA)
Cite as Authors (Year) Title. American Mineralogist, in press.
(DOI will not work until issue is live.) DOI: http://dx.doi.org/10.2138/am-2016-5563

1046 **Table 1.** ^{13}C NMR chemical shift for various crystalline and amorphous carbon materials.

Sample	Carbon species	Peak position (ppm)	FWHM (ppm)	B_0 (T)	Spin rate (kHz)	Ref.†
Amorphous carbon (rf sputtering)	sp^2-like carbon	130	200	2.35	4.4	(1)
	sp^3-like carbon	62	~ 26.8			
Amorphous carbon (PLD)	sp^2-like carbon	137.8	41.3	9.4	15	(2)
	sp^3-like carbon	67.5	49.8			
Carbon nanotubes	single-walled nanotubes with 2.4 at% Rh/Pd	124		9.4	11.7	(3)
	single-walled nanotubes (pure)	118.8		4.7		(4)
	single-walled nanotubes (with adsorbed CO)	123.8				
	double-walled nanotubes	116.3				
	multi-walled nanotubes (15±5 walls)	106.1				
	multi-walled nanotubes (60±10 walls)	102.3				
Graphene	graphene	123		8.46	9.4	(5)
Fullerene black + C_{60}	C_{60}	142.6	0.7	7.05	5	(6)
	C_{70}	129.9, 144.7, 146.9, 149.7			6.6	
	polyynic carbon chain	~ 70				
Carbon black	aromatic C=C	126		6.35	5.3	(7)
	C=O	167				
	aliphatic C-C	20				

1047

1048 † (1) Pan et al. (1991); (2) Alam et al. (2003); (3) Tang et al. (2000); (4) Abou-Hamad et al.
1049 (2011); (5) Si and Samulski (2008); (6) Kanowski et al. (1997); (7) Jäger et al. (1999)

1050

APPENDIX

A1. Solubility of carbon into crystalline silicates at high pressure up to 25 GPa

The solubility and detailed structure around carbon species in crystalline silicates are often difficult to probe. This is partly because the solubility of the carbon species is relatively low, on the order of 0.01 to 10 ppm (Keppler et al., 2003; Shcheka et al., 2006), and suitable probes are limited. Furthermore, the solubility measurement is often complicated by several extrinsic factors including presence of excess carbon in the grain boundary; the resulting carbon solubility in silicate crystals varied from the order of 0.01 ppm to 2500 ppm (Freund et al., 1980; Keppler et al., 2003; Mathez et al., 1984; Shcheka et al., 2006; Tingle and Aines, 1988; Tsong and Knipping, 1986; Tsong et al., 1985) .

Despite the challenge, previous efforts have provided some insights into carbon species in various silicate crystals at pressures up to 26 GPa (Keppler et al., 2003; Taylor et al., 1990) (Keppler et al., 2003; Shcheka et al., 2006). The carbon solubility in the silicates does not show a great variation depending on the types and composition of the crystals. The estimated total carbon content in the Mg-silicates apparently increases with increasing pressure, but the formation of Mg-perovskite phase leads to a reduction in the carbon solubility in silicate (Keppler et al., 2003; Shcheka et al., 2006). Table A1 summarizes the estimated carbon solubility in the various silicate polymorphs in a pressure range of 1–26 GPa (Keppler et al., 2003; Shcheka et al., 2006). The solubility of carbon in enstatite at 1.5 GPa varies from 0.05 ppm to 4.7 ppm, which may reside from the carbon contents in the grain boundaries.

This is a preprint, the final version is subject to change, of the American Mineralogist (MSA)
Cite as Authors (Year) Title. American Mineralogist, in press.
(DOI will not work until issue is live.) DOI: http://dx.doi.org/10.2138/am-2016-5563

1073 **Table A1 |** Solubility of carbon species in crystalline silicates with varying composition, pressure,
1074 and temperature, as reported in previous studies.

Composition	Pressure (GPa)	Temperature (°C)	Duration (h)	Solubility (wt ppm)	Ref.*
Enstatite ($MgSiO_3$)	1.5	900–1100	96–168	0.05(1)–0.19(4)	(1)
	1.5	900	96	3.0–4.7	(2)
	6	1100	5	0.38(3)–0.44(3)	(1)
	16	1400	10	0.69(6)–0.80(6)	
Olivine [$(Mg,Fe)_2SiO_4$]	1	1200	34	Not detected	(1)
	1.5	900–1100	144–168	<0.09–0.38(9)	
	1.5	1200	68	0.14(2)–0.25(2)	
	2	1200	71	0.34(4)	
	3.5	1200	71	0.29(4)–0.54(6)	
	7	1200	10	3.27(29)–3.90(68)	
	11	1200	10	11.57(34)–12.75(53)	
Diopside ($CaMgSi_2O_6$)	1.5	900–1100	96–168	<0.01–0.16(2)	(1)
	1.5	900	168	0.4–0.5	(2)
	6	1100	8	1.45(7)–1.60(6)	(1)
Pyrope ($Mg_3Al_2Si_3O_{12}$)	6	1300	10	0.85(5)–0.87(5)	(1)
	6	1300	10	1.9–2.1	(2)
	9	1300	10	0.83(6)–1.27(7)	(1)
	10	1300	6	0.82(4)–0.96(5)	
Spinel ($MgAl_2O_4$)	1.5	1100	168	<0.02	(1)
	1.5	1100	168	Not detected	
Wadsleyite [$(Mg,Fe)_2SiO_4$]	16	1400	10	<0.04–0.04(1)	(1)
	17	1400	4	<0.05	
Ringwoodite [$(Mg,Fe)_2SiO_4$]	21	1200	10	0.04(1)	
	23	1200	4	<0.07–0.10(2)	
Ilmenite ($MgSiO_3$)	25	1400	10	<0.08	(1)
Bridgmanite (Perovskite) ($MgSiO_3$)	25	1400	10	<0.07	(1)
	26	1400	3	<0.05	

1075

1076 * (1) Shcheka et al. (2006); (2) Keppler et al. (2003)

This is a preprint, the final version is subject to change, of the American Mineralogist (MSA)
Cite as Authors (Year) Title. American Mineralogist, in press.
(DOI will not work until issue is live.) DOI: http://dx.doi.org/10.2138/am-2016-5563

A2. The presence of $^{13}CH_4$ in carbon-bearing enstatite by using proton decoupling

Figure A1 shows ^{13}C MAS NMR spectrum for carbon-bearing enstatite with decoupling power of 33 kHz and spinning speed at 11 kHz. Any decrease in the peak width for the peak ~ -9 ppm in Fig. 3 has not been observed. The result may indicate that the small feature at ~ -9 ppm is from background signal.

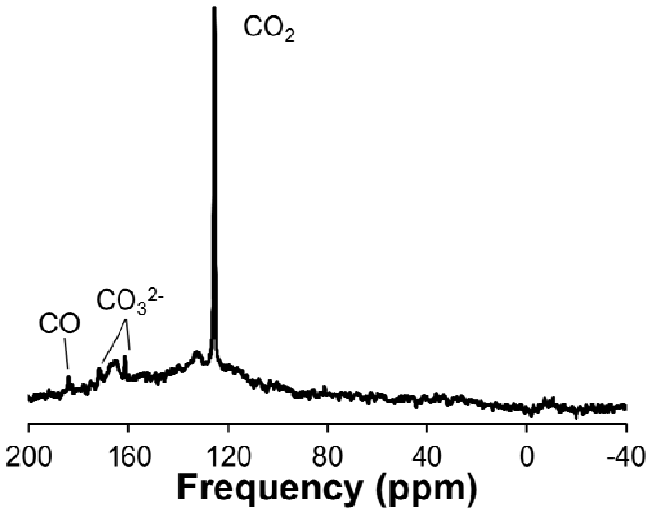

Figure A1| ^{13}C MAS NMR spectrum for carbon-bearing enstatite under proton decoupling with an applied Lorentzian broadening factor of 40.

A3. Effect of residual H in the pressure-induced carbon peak shifts in the amorphous carbon

Protonation into carbon could also affect the observed change in peak position of amorphous carbon under compression. We collected ^{1}H MAS NMR spectra for the compressed and uncompressed amorphous carbon in order to identify whether there would be any ^{1}H reservoir and potential protonation of the sample. The spectra were collected on a Varian NMR system (9.4 T) at a Larmor frequency of 400.01 MHz (3.2 mm double-resonance Varian probe). Single-pulse acquisition with a pulse length of 1.6 μs (radio frequency tip angle of about 30° for solids) was used with a recycle delay of 5 s and spinning speeds of 14 kHz. The potential results would allow us to confirm whether the observed changes in the peak shift is due to residual proton from the H_2O added during the sample synthesis. Figure A1 shows the ^{1}H MAS NMR spectra for ^{13}C-enriched uncompressed and compressed amorphous carbon and those for rotor and stator backgrounds. ^{1}H MAS NMR spectra for rotor and stator background show a broad peak at ~ 7 ppm. The shoulder at ~ -1 ppm is observed for uncompressed amorphous carbon. The assignment of the feature is not trivial, yet previous ^{1}H NMR study for the amorphous carbon under milling showed a broad feature near ~ -1 ppm, assigned to hydrogenated amorphous carbon (Shindo et al., 2011). No noticeable proton peak is observed for compressed amorphous carbon, suggesting the absence of proton reservoir in compressed amorphous carbon. The result confirms that the proton signal from rotor and stator background is far much greater than those from the amorphous carbon and there is no noticeable proton reservoir for the compressed carbon. Taking into consideration negligible H content in the compressed amorphous carbon, it is expected that ^{1}H-^{13}C cross-polarization NMR does not probe the H-C interaction within the amorphous carbon. Indeed, our preliminary ^{1}H-^{13}C cross-polarization NMR spectra for the

This is a preprint, the final version is subject to change, of the American Mineralogist (MSA)
Cite as Authors (Year) Title. American Mineralogist, in press.
(DOI will not work until issue is live.) DOI: http://dx.doi.org/10.2138/am-2016-5563

sample and rotor showed that the most of the signals are from the rotor and stator. The current results again confirm the pressure-induced peak shift were not affected by the proton in the sample.

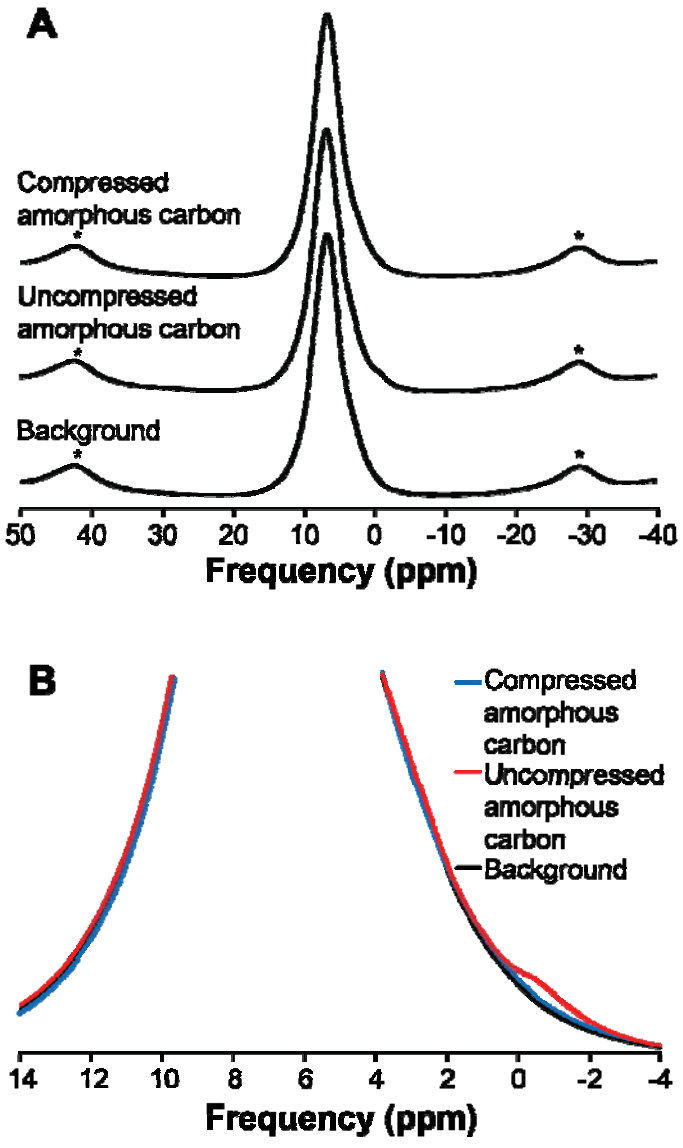

Figure A2| (A) ^{1}H MAS NMR spectra for compressed amorphous carbon, amorphous carbon, and rotor-stator background. Asterisks denotes spinning sidebands. (B) Expanded ^{1}H MAS NMR spectra for the samples as labeled.

This is a preprint, the final version is subject to change, of the American Mineralogist (MSA)
Cite as Authors (Year) Title. American Mineralogist, in press.
(DOI will not work until issue is live.) DOI: http://dx.doi.org/10.2138/am-2016-5563

A4. Detection limit on ^{13}C MAS NMR under proton decoupling

Figure A3 shows the ^{13}C MAS NMR spectra for ADM-SiO_2 mixtures with varying X_{ADM} ratio with decoupling power of 33 kHz. The spectra show that proton decoupling indeed improves signal-to-noise ratio and ^{13}C MAS NMR spectrum for the sample with X_{ADM} =1/259, ~43 ppm can be obtained. See Figure 7 for the calibration results based on the decoupling experiments.

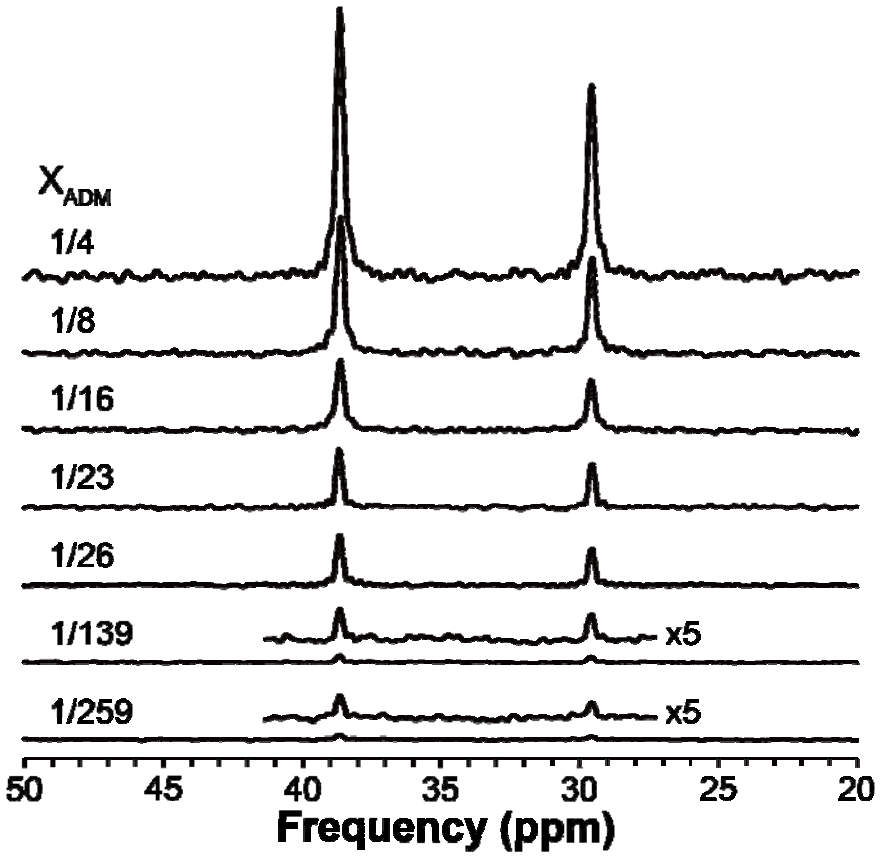

Figure A3| ^{13}C MAS NMR spectra for ADM-SiO_2 mixtures with varying X_{ADM} ratio with decoupling power of 33 kHz.

This is a preprint, the final version is subject to change, of the American Mineralogist (MSA)
Cite as Authors (Year) Title. American Mineralogist, in press.
(DOI will not work until issue is live.) DOI: http://dx.doi.org/10.2138/am-2016-5563

A5. The characteristics of the ^{13}C peak width of various carbonate species

Figure A4 shows the ^{13}C static NMR spectra of 1 M $Na_2CO_3(aq)$ and 1 M $(Na_2{}^{13}CO_3+NaHCO_3)(aq)$, and ^{13}C MAS NMR spectra of calcite and natrite to explore the characteristics of their peak shape in the ^{13}C NMR spectra. The spinning speed for calcite and natrite is 14.7 kHz. The FWHM of calcite and natrite peak in ^{13}C MAS NMR spectra are 0.48 and 0.42 ppm with an employed Lorentzian broadening factor of 10, respectively. The FWHM of 1 M $Na_2{}^{13}CO_3(aq)$ and 1 M $(Na_2{}^{13}CO_3+NaHCO_3)(aq)$ in ^{13}C MAS NMR spectra are 0.48 and 0.48 ppm with an employed Lorentzian broadening factor of 10, respectively. The FWHM of carbonates peaks in the carbon-bearing enstatite at 161.2, 170.9, and 173.3 ppm are 0.29, 0.37, and 0.35 ppm with a Lorentzian broadening factor of 10, respectively. Therefore, it is difficult to identify their phases (either solid or liquid) based only on their peak widths due to the similarity in FWHM of carbonate minerals and carbonate ions in aqueous solution. Although spectra for aqueous solution collected without spinning at the magic angle, we note that ^{13}C liquid-state NMR under MAS may not reduce the FWHM of the carbonate species in aqueous solution.

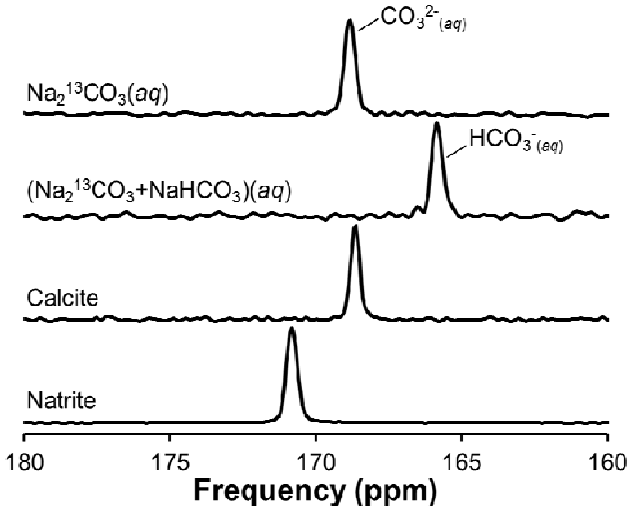

Figure A4| ^{13}C NMR spectra for 1 M $Na_2{}^{13}CO_3(aq)$, 1 M $(Na_2{}^{13}CO_3+NaHCO_3)(aq)$, calcite, and

natrite with an employed Lorentzian broadening factor of 10.

This is a preprint, the final version is subject to change, of the American Mineralogist (MSA)
Cite as Authors (Year) Title. American Mineralogist, in press.
(DOI will not work until issue is live.) DOI: http://dx.doi.org/10.2138/am-2016-5563

A6. Estimation of the detection limit of carbonate phase in the enstatite-calcite mixture using conventional XRD

In order to test the detectability of carbonate species in the silicate matrix, we collected XRD patterns from enstatite-calcite mixture with varying concentration of carbonate phase (on Rigaku MiniFlex600, using Cu*Kα* X-rays, voltage of 40 kV, current of 15 mA, a 2θ range of 10°–60°, a step width of 0.01°, and scan rate of 0.4 s/point). Figure A5 shows the XRD patterns of enstatite-calcite mixture with varying $X_{calcite}$ from 0 to 1/32. The calcite (104) peak (red line at 29.4°) intensity can be seen up to $X_{calcite}$=1/256 (~ 0.39 wt%) sample, which is the detection limit with the employed instrument and conditions used in the study. The estimated carbonate concentration is much smaller than the current detection limit of XRD.

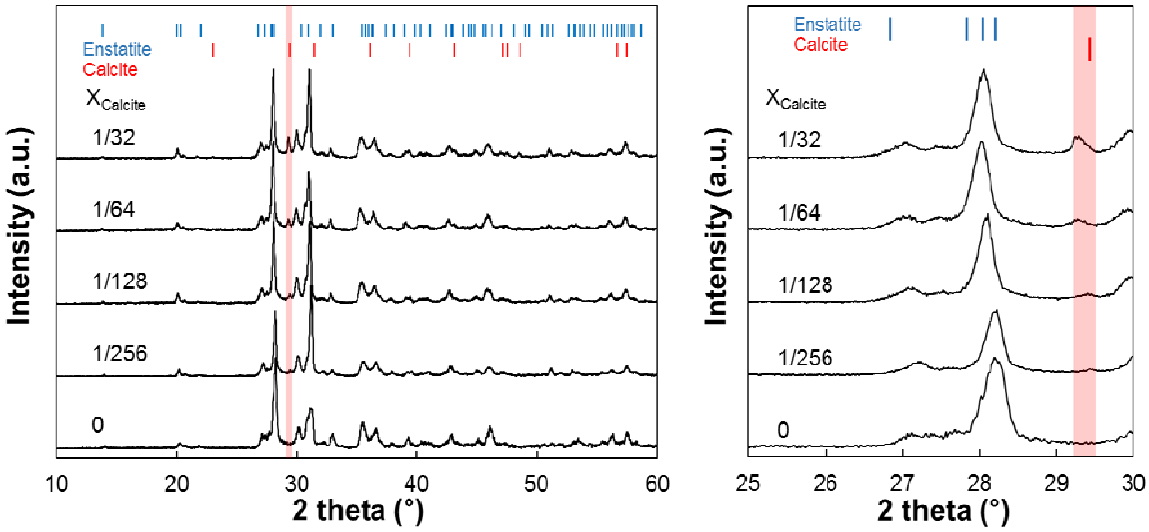

Figure A5| XRD patterns of enstatite-calcite mixture with varying $X_{calcite}$ from 0 to 1/32. Blue and red lines on the top of the figure refer to XRD patterns of enstatite and calcite, respectively. A red area show the decrease of calcite intensity with decreasing $X_{calcite}$ in the sample.